Chemical Engineering Journal 546 (2026) 179800

Contents lists available at ScienceDirect

Chemical Engineering Journal

journal homepage: www.elsevier.com/locate/cej

Biomimetic organo-specific scaffolds reveal lineage-specific adaptations of breast cancer cells in bone metastasis

Chiara Spadazzi [a,*], Silvia Vanni [a], Alessandro De Vita [a], Claudia Cocchi [a,*], Sofia Gabellone [a], Giacomo Miserocchi [a], Chiara Calabrese [a], Sofia Dellavalle [a], Oneda Cani [a], Lucas Moron Dalla Tor [b], Michela Tebaldi [c], Ane Urigoitia-Asua [f,g], Dorleta Jimenez de Aberasturi [f,h], Erlantz Lizundia [i], Oihane Mitxelena-Iribarren [j], Amaia Cipitria [h,j], Antonino Musolino [k], Chiara Casadei [k], Giulia Sbanchi [a], Denisa Toma [a], Eliana Capecchi [d], Raffaele Saladino [d], Toni Ibrahim [e], Laura Mercatali [e,1], Chiara Liverani [a,1]

[a] *Preclinic and Osteoncology Unit, Bioscience Laboratory, IRCCS Istituto Romagnolo per lo Studio dei Tumori (IRST) "Dino Amadori", Via P. Maroncelli 40, 47014, Meldola, Italy*
[b] *Department of Medicine and Surgery, University of Parma, Viale Antonio Gramsci, 14, 43126, Parma, Italy*
[c] *Unit of Biostatistics and Clinical Trials, IRCCS Istituto Romagnolo per lo Studio dei Tumori (IRST) "Dino Amadori", Via P. Maroncelli 40, 47014, Meldola, Italy*
[d] *Department of Ecological and Biological Sciences, University of Tuscia, Largo dell'Università snc, 01100, Viterbo, Italy*
[e] *Osteoncology, Bone and Soft Tissue Sarcomas and Innovative Therapies Unit, IRCCS Istituto Ortopedico Rizzoli, Via G. C. Pupilli 1, 40136, Bologna, Italy*
[f] *CIC biomaGUNE Basque Research and Technology Alliance (BRTA), Paseo de Miramon 194, Donostia-San Sebastián, 20014, Spain*
[g] *POLYMAT Applied Chemistry Department, Faculty of Chemistry, University of the Basque Country UPV/EHU, Donostia-San Sebastián, 20018, Spain*
[h] *IKERBASQUE Basque Foundation for Science, Bilbao, 48009, Spain*
[i] *Life Cycle Thinking Group, Department of Graphic Design and Engineering Projects, Faculty of Engineering in Bilbao, University of the Basque Country (UPV/EHU), Bilbao, 48013, Spain*
[j] *Group of Bioengineering in Regeneration and Cancer, Biogipuzkoa Health Research Institute, San Sebastián, Spain*
[k] *Medical Oncology, Breast & GYN Unit, IRCCS Istituto Romagnolo per lo Studio dei Tumori (IRST) "Dino Amadori", Via P. Maroncelli 40, 47014, Meldola, Italy*

ARTICLE INFO

Keywords:
Bone metastasis
Breast cancer
Extracellular matrix (ECM)
Biomimetic scaffolds

ABSTRACT

Bone metastasis is a major clinical complication of breast cancer, regulated by dynamic interactions between disseminated tumor cells and the bone extracellular matrix (ECM). Experimental models that accurately replicate the biochemical, structural, and mechanical features of the bone niche remain limited. Here, we engineered three-dimensional organo-specific ECM scaffolds to investigate how bone-mimetic matrices regulate breast cancer cell behavior, phenotypic plasticity, and therapeutic response. Collagen-based scaffolds mimicking primary breast tumor ECM and collagen–hydroxyapatite (coll-HA) scaffolds reproducing bone ECM were developed. Physicochemical characterization confirmed that coll-HA scaffolds showed effective hydroxyapatite integration, trabecular-like organization, physiological porosity, and elastic properties consistent with the bone metastatic niche. Upon cellularization with breast cancer cells, the scaffolds reproduced key histological features and tumor cell morphologies observed in human bone metastasis. Using four breast cancer cell lines representative of distinct molecular subtypes and degree of bone tropism, we demonstrated that organo-specific ECMs profoundly influence cell growth dynamics and phenotypic plasticity. In the bone-mimetic niche, tumor cells exhibited reduced proliferation and adopted subtype-specific epithelial–mesenchymal states. Transcriptomic profiling revealed lineage-dependent metabolic reprogramming and modulation of bone metastasis-associated signaling. The bone-mimetic ECM also enhanced tumor cell sensitivity to bone-targeted therapies and osteoclastogenic ability, highlighting the role of tumor–ECM interactions in shaping the osteolytic microenvironment. Collectively, organo-specific ECM scaffolds provide a physiologically relevant platform to study breast cancer adaptation to the bone microenvironment, offering mechanistic insights into microenvironment-driven plasticity,

* Corresponding authors.
E-mail addresses: chiara.spadazzi@irst.emr.it (C. Spadazzi), claudia.cocchi@irst.emr.it (C. Cocchi).
[1] These authors contributed equally to this work as last authors.

https://doi.org/10.1016/j.cej.2026.179800
Received 31 March 2026; Received in revised form 14 July 2026; Accepted 21 July 2026
Available online 23 July 2026

metabolism and therapeutic vulnerabilities, with implications for improving treatments for bone metastatic disease.

1. Introduction

Breast cancer is the most commonly diagnosed cancer in the female population and the second leading cause of death in women [1]. Unlike primary tumors, which are frequently curable with local surgery or radiation, metastasis accounts for the majority of cancer-related deaths, despite recent therapeutic advancements [2]. The spread of primary cancer cells from the original tumor involves sequential and interconnected steps, making cancer metastasis a complex process. Breast cancer metastasis exhibits organotropisms, with the bone as one the most frequent sites, accounting for about 65–75% of advanced cases [2,3]. Different molecular breast cancer subtypes exhibit varying degrees of propensity to develop bone metastasis [4,5]. The combination of cell-intrinsic features and the influence of the microenvironment, both at the primary and metastatic sites, guide dissemination to bone rather than to other organs [4,5]. Moreover, clinical evidence indicates that when breast cancer spreads to the bones, there is a high risk of later metastasis to multiple organs [6,7]. This appears to be driven by the interaction between cancer cells and resident cells, as well as to cytokines released within the bone microenvironment [8,9]. These interactions not only dictate the bone to support cancer cell survival but also strengthen metastatic cells, facilitating their further spread to other organs. Bone microenvironment is a highly heterogeneous and dynamic niche that hosts different bone cells (osteoblasts, osteoclasts and their precursors), stromal cells, hematopoietic and immune cells, adipocytes, endothelial and fibroblasts cells, which orchestrate the bone remodeling process and immune function during the development [10,11]. All these cells are surrounded by an extracellular matrix (ECM) which is composed of organic and inorganic components [12,13]. The main organic component is represented by type I collagen fibrils, which give the strength and stiffness to the bone matrix and the structural support for cell attachment. Collagen fibers are strictly organized in a hierarchical and directional manner corresponding to cellular orientation. The most represented inorganic component of the bone matrix is the hydroxyapatite crystals, which regulate the bone matrix mineralization. It has been shown that the structure and orientation of the hydroxyapatite crystals, in conjunction with the collagen fibrils, are critical for bone matrix organization [12,13]. In pathological conditions, the alignment of apatite crystals and collagen can be altered, affecting cell behavior and differentiation. Emerging evidence highlights the key role of the bone ECM in metastatic progression [14]. Its biochemical and mechanical properties can affect the plasticity of disseminated cancer cells, which adapt to the hostile microenvironment and increase their growth and survival [15]. Moreover, tumor cells can disseminate early to bone, also during primary tumor formation and enter a state of dormancy in which they proliferate less and assume stem-like properties [16–18]. Microenvironmental conditions are key determinants of tumor-cell latency and stemness and, as a direct consequence, of sensitivity to drugs [19]. The identification of how the bone ECM influences these processes remains essential for developing effective treatment strategies for metastatic patients [20]. Different experimental approaches have been attempted to model the interactions between tumor cells and microenvironment during the sequential stages of tumor metastasis [21,22]. Here we developed an in vitro platform based on tailored three-dimensional matrices that reproduce the ECM composition of primary breast and bone metastatic lesions, enabling us to isolate the contribution of organo-specific ECM to cancer cell behavior. Using this system, we demonstrated that the ECM is not merely a structural support but an active regulator of cancer cell adaptation, inducing lineage-dependent changes in breast cancer cell phenotype, transcriptional programs, crosstalk with osteoclasts, and responsiveness to bone-targeted therapies.

2. Results

2.1. Structural and physicochemical properties of ECM- mimicking scaffolds

To reproduce the native ECM of primary breast tumors we exploited a previously developed three dimensional (3D) collagen scaffold model, which recapitulates the aggressiveness and heterogeneity of breast cancer cells [23,24]. To reproduce the bone-like ECM, we next synthesized scaffolds composed of type I collagen and hydroxyapatite in a ratio of 30:70 reflecting the healthy bone tissue [12]. Both scaffolds were synthetized with a dimension of 9 mm of diameter and 2 mm of thickness (Fig. 1a). Attenuated total reflection Fourier Transform Infrared (ATR-FTIR) analysis confirmed the presence of collagen in the 3D scaffold by its characteristic amide bands and CH_2 stretching vibrations, with a broad –OH band around 3300 cm^{-1}. In the collagen–hydroxyapatite (coll-HA) scaffold, the spectrum was dominated by HA features, while collagen (coll) peaks showed a slight leftward shift and reduced intensity. Amide *I*, II, and III shifted to 1654, 1546, and 1243 cm^{-1}, respectively, indicating stronger intermolecular interactions and reduced molecular flexibility (Fig. 1b). Field Emission Scanning Electron Microscope (FE-SEM) analysis confirmed that both materials exhibit a porous architecture, with pore sizes ranging approximately from 20 to 100 μm (Fig. 1c). The X-ray diffraction (XRD) patterns of the coll-HA scaffold matched with the standard International Centre for Diffraction Data (ICDD) database for calcium phosphate hydroxide (card #01–074-0565), confirming the successful incorporation of HA (Fig. 1d). The main diffraction peaks, suggesting the material's hexagonal crystal structure, were observed at 2θ: 26.0° (002), 29.1° (210), 31.9° (211), 32.3° (112), 33.1° (300), 40.0° (221), 46.8° (222), 49.6° (213), and 53.3° (004) [25]. The crystalline degree (X_C) was 49.1% and the mean crystalline size was 39.52 nm, likely due to collagen presence, as pure HA typically shows approximately 52.0 nm crystallites. Finally, the interplanar distance for the lattice spacing of (211) was 2.803 Å, in excellent agreement with values reported in literature (2.81 Å) [26].

Micro-computed tomography (μCT) was utilized to quantitatively analyze the physical and architectural properties of the scaffolds (Fig. S1a). Incorporation of HA, led to a significant increase (174.0 ± 20.5 mm^3) in the overall scaffold volume (Vtotal) compared to that of coll scaffold (126.8 ± 14.1 mm^3) (Fig. 1e). Coll-HA scaffolds also showed a substantially greater solid volume (Vsolid), with a mean of 104.2 ± 14.8 mm^3, compared to 49.1 ± 15.8 mm^3 for coll scaffolds. This represents the double solid material content when HA was incorporated into the matrix. Crucially, despite this marked increase in Vtotal and Vsolid, the absolute volume of void space (Pore Volume, Vpore) remained constant between coll and coll-HA scaffolds. Coll scaffolds had a mean porosity of 77.6 ± 6.6 mm^3, while coll-HA scaffolds showed 69.8 ± 5.8 mm^3, indicating that total void volume did not markedly change despite the larger overall scaffold size in coll-HA matrix (Fig. 1e). When analyzing the scaffold solid phase and the porosity as a percentage of Vtotal, the solid fraction increased significantly from 38.3 ± 8.2% in coll scaffolds to 59.8 ± 1.5% in coll-HA scaffolds, that also exhibited a lower percent porosity (ca 40.2% vs. 61.7%) and were notably denser (Fig. 1f). The observed constant Vpore despite an increased Vtotal and Vsolid suggests that the HA particles were successfully integrated into the collagen matrix rather than occupying existing void spaces. The porosity values of coll-HA were close to the range reported to support nutrient diffusion, cell penetration, and proliferation throughout the entire scaffold's structure [27].

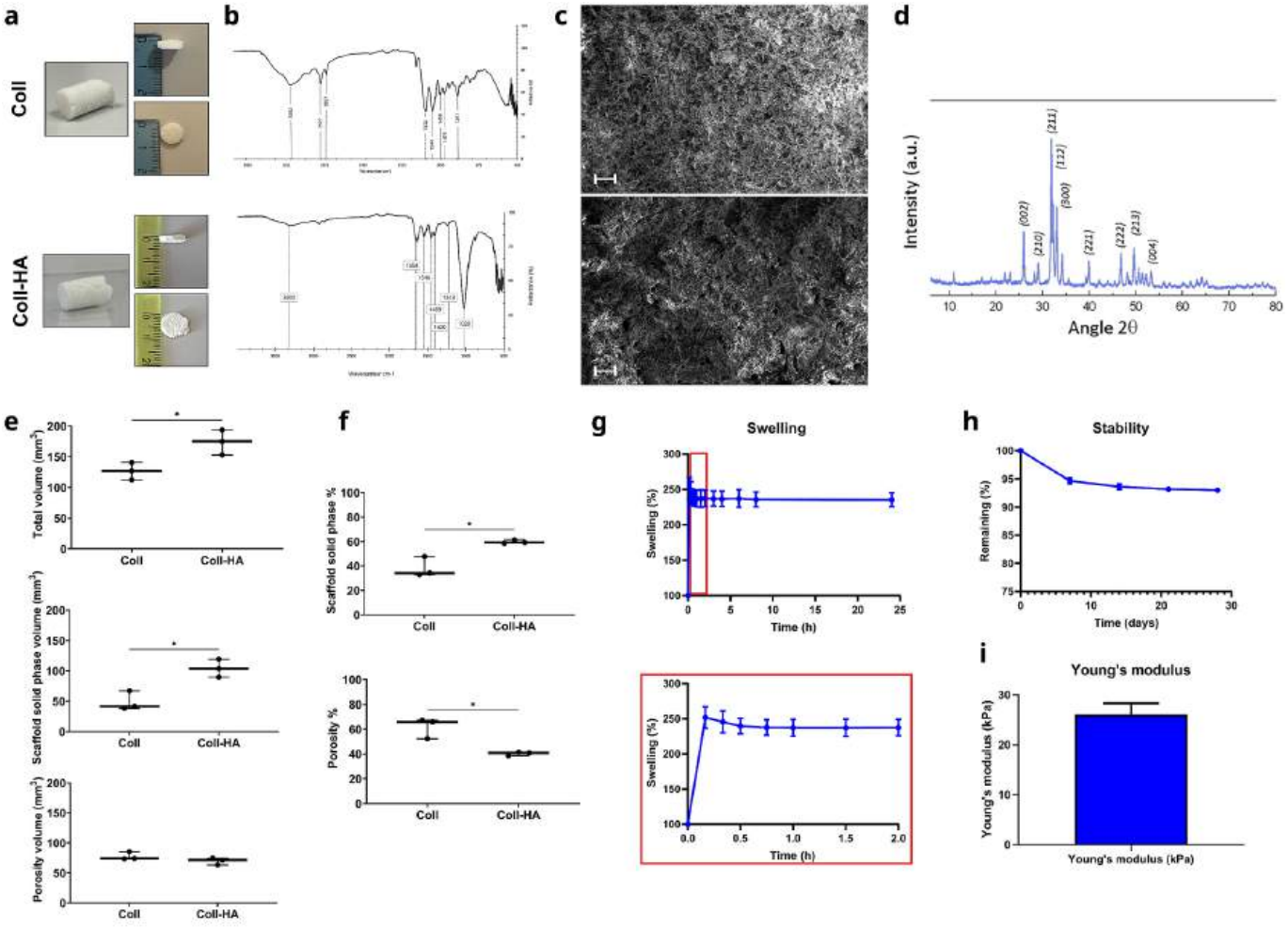

(caption on next page)

Fig. 1. Characterization of coll and coll-HA scaffolds. (a) Macroscopic images of coll and coll-HA scaffolds, showing shape and dimensions. (b) Attenuated total reflection Fourier-transform infrared (ATR-FTIR) spectrum of coll and coll-HA scaffolds, indicating their chemical composition. (c) Field Emission Scanning electron microscopy (FE-SEM) images of the scaffolds' surface, highlighting the microstructure. For coll scaffold image scale bar = 200 μm, for coll-HA scale bar = 40 μm. (d) X-Ray Diffraction (XRD) analysis of coll-HA scaffolds. (e) Quantification of the total volume, solid phase volume and porosity volume, obtained for coll and coll-HA scaffolds with the microCT imaging and the ORS Dragonfly software, measured in mm^3. Statistical analysis was performed using unpaired *t*-test and Mann–Whitney for porosity volume. (f) Percentage of the scaffolds' solid phase and porosity with respect to the total volume. Statistical analysis was performed using unpaired *t*-test (with Welch's correction). (g) Swelling of coll-HA scaffolds in PBS at 37 °C for 24 h (left) with zoom of the first 2 h (right). (h) Scaffold stability for 28 days. (i) Young's modulus of coll-HA scaffolds obtained by compression test. (j) Histological comparison between the bone metastasis from ER+ breast cancer (left) and engineered 3D coll-HA scaffold seeded with ER+ MCF7 breast cancer cells (right), stained with hematoxylin and eosin (H&E). Images were taken at 4× magnification, with insets magnified to 40×. The scale bar represents 600 μm for 4× images and 60 μm for 40× images. The model enables to reproduce the bone structure and architecture. Statistical significance ($n = 3$) is indicated as $^*P < 0.05$. Error bars show standard deviation (SD).

The swelling analysis over 24 h demonstrated that coll-HA scaffolds achieve full hydration rapidly, reaching a maximum swelling value of 251.68% ± 5.41% within the first 10 min from their dried state (Fig. 1g). A slight decrease in swelling was observed shortly after the initial time points (237.22% ± 11.94% after 1 h), which is likely attributable to the dissolution of a small fraction of uncrosslinked material. Subsequently, the swelling ratio stabilized, maintaining 235.62% ± 9.8% after 24 h. The high level of swelling and water retention is a key functional property that enables effective hydration. The stability of the scaffolds in Phosphate-Buffered Saline (PBS) was robust, maintaining 93.02% ± 0.21% of their mass over the study period (Fig. 1h). Samples initially lost approximately 5% of their dry mass upon the submersion in PBS. This loss corresponds to the elution of the uncrosslinked collagen chains or low-molecular-weight oligomers. Then, scaffolds remained highly stable, losing only an additional 1.6% of their dry mass over the subsequent 21 days, with over 90% mass being preserved after 28 days, demonstrating an excellent long-term hydrolytic stability in a physiological environment. To further corroborate the stability of the crosslinked network and the potential release of residual crosslinker over time, a leachate assay was performed by monitoring 1, 4-butanediol diglycidyl ether (BDDGE) release from the scaffolds over time. No detectable chromatographic signal attributable to BDDGE at any investigated time point was found (data not shown) providing evidence that unreacted or weakly bound crosslinker was effectively removed during post-synthesis washing steps, while the fraction incorporated into the scaffold remained chemically bound within the matrix network. Compression testing of coll-HA scaffolds revealed stress-strain curves with a linear region (0% - 30% strain characteristic of the elastic deformation), followed by a plateau phase (30% - 65% strain, where the collagen structure starts the permanently plastic deformation) and a densification phase (65% - 90%, characterized by the collapse of the structure due to excess tension) (Fig. S1b, c). The scaffolds presented a Young's modulus of 26.02 kPa ± 2.26 kPa in hydrated state corresponding to an elastic and porous matrix (Fig. 1i). This value is in the range reported for the bone tissue microenvironment surrounding breast cancer cells in an in vivo mouse model [28].

Finally, we compared the histology of coll-HA scaffolds cellularized with estrogen receptor positive (ER+) breast cancer cells with a bone metastatic lesion from an ER+ breast cancer patient. The coll-HA scaffolds displayed a dense network of eosinophilic collagen fibers interconnected with amorphous basophilic HA deposits, forming a porous, trabeculae-like structure. The metastatic lesion showed an infiltrative neoplastic process within the trabecular bone architecture which was extensively altered. Tumor cells were morphologically similar across both samples, forming nests and cords of epithelioid cells with moderate eosinophilic cytoplasm, round-to-oval nuclei with fine chromatin and small nucleoli, and infrequent mitoses, consistent with the indolent proliferative profile of ER+ breast cancer in metastatic contexts. Porous architecture facilitated tumor dissemination, with tumor occupying 50–70% of fields and compressing residual native elements (marrow in patient; scaffold voids in models). Overall, these findings indicate that our model captures relevant architectural and structural features of the bone matrix and of cancer cells morphology and organization (Fig. 1j).

2.2. Organo-specific ECMs alter breast cancer cell growth dynamics and plasticity

We next investigated how different ECMs affect breast cancer cell behavior by comparing responses in coll (breast-mimetic) versus coll-HA (bone-mimetic) matrices. Four cell lines, representative of distinct breast cancer subtypes with different molecular patterns and clinical behavior, were selected: MDA-MB-231, a triple negative cell line connected to high grade and aggressive disease, the bone metastatic SCP2 cell line, a subclone of MDA-MB-231 in vivo isolated to preferentially metastasize to bone [29], the ER+ luminal A MCF7 cell line, connected to a more indolent and less aggressive disease and the ER+, progesterone receptor-positive (PR+), and HER2/neu overexpressing luminal B BT-474 cell line. First, we compared their cell growth dynamics, morphology and disposition in a time course experiment of 10 days. In the coll scaffold MCF7, MDA-MB-231 and SCP2 aligned over the matrix fibers, while in 3D coll-HA cells appeared homogeneously dispersed (Fig. 2a). In contrast, BT-474 exhibited a nested organizational pattern in both scaffolds. All cell lines displayed a round epithelial-like morphology within the coll-HA scaffold as demonstrated by cell circularity analysis (Fig. S2a). In contrast, MDA-MB-231 and MCF7 cultured in the coll scaffold appeared to have a spindle-shaped mesenchymal-like morphology. Circularity analysis revealed a higher proportion of elongated cells (range < 0.4) on the coll scaffold compared to the coll-HA scaffold for MDA-MB-231 ($P = 0.007$), whereas MCF7 cells did not exhibit this difference. The proliferative capacity for MDA-MB-231, SCP2 and MCF7 cells was significantly reduced in the presence of HA at all time points following 72 h of culture. BT-474 proliferation was not significantly influenced by the different matrices, except at day 10, where increased growth was observed on the coll-HA scaffolds. This observation was supported by ATP quantification, which revealed significantly lower levels of metabolically active cells in MDA-MB-231, MCF7, and SCP2 cultured within the coll-HA scaffold compared with coll alone, particularly at later time points. BT-474 cells did not exhibit significant alterations in metabolic activity, with the exception of a transient decrease in active cells at day 7 (Fig. 2b). Interestingly, ATP production decreased after 72 h in cells cultured within coll-HA scaffolds, suggesting also a potential shift to alternative metabolic pathways. RNA-sequencing data and gene expression analysis of key epithelial-mesenchymal transition (EMT) and mesenchymal-epithelial transition (MET) markers at 24 h, 72 h and 7 days of culture revealed distinct phenotypic shifts induced by coll-HA ECM compared to the coll matrix (Fig. 2c, Figs. S3a and S4). MDA-MB-231 cells, which are typically mesenchymal, exhibited at 7 days a significant upregulation of CDH1 (E-cadherin), that is associated with an epithelial phenotype ($P = 0.0121$), and a downregulation of VIM (vimentin), SNAI1 and THBS1 ($P = 0.0379$ and $P = 0.0216$ for VIM at 24 h and 72 h, respectively, $P = 0.0077$ for SNAI1 at 72 h, and $P = 0.027$ at 72 h for THBS1) (Fig. 2c). RNA sequencing analysis of transcription factors (TFs)-dependent gene expression indicated significant activation of the GATA3 regulatory program, a master determinant of epithelial identity, alongside downregulation of MYC- and HIF-1α–associated gene expression (Fig. S3a). SCP2 cells display a significant downregulation of mesenchymal markers as CD44 ($P = 0.0085$ at 7 days), VIM ($P = 0.0427$ at 24 h and P

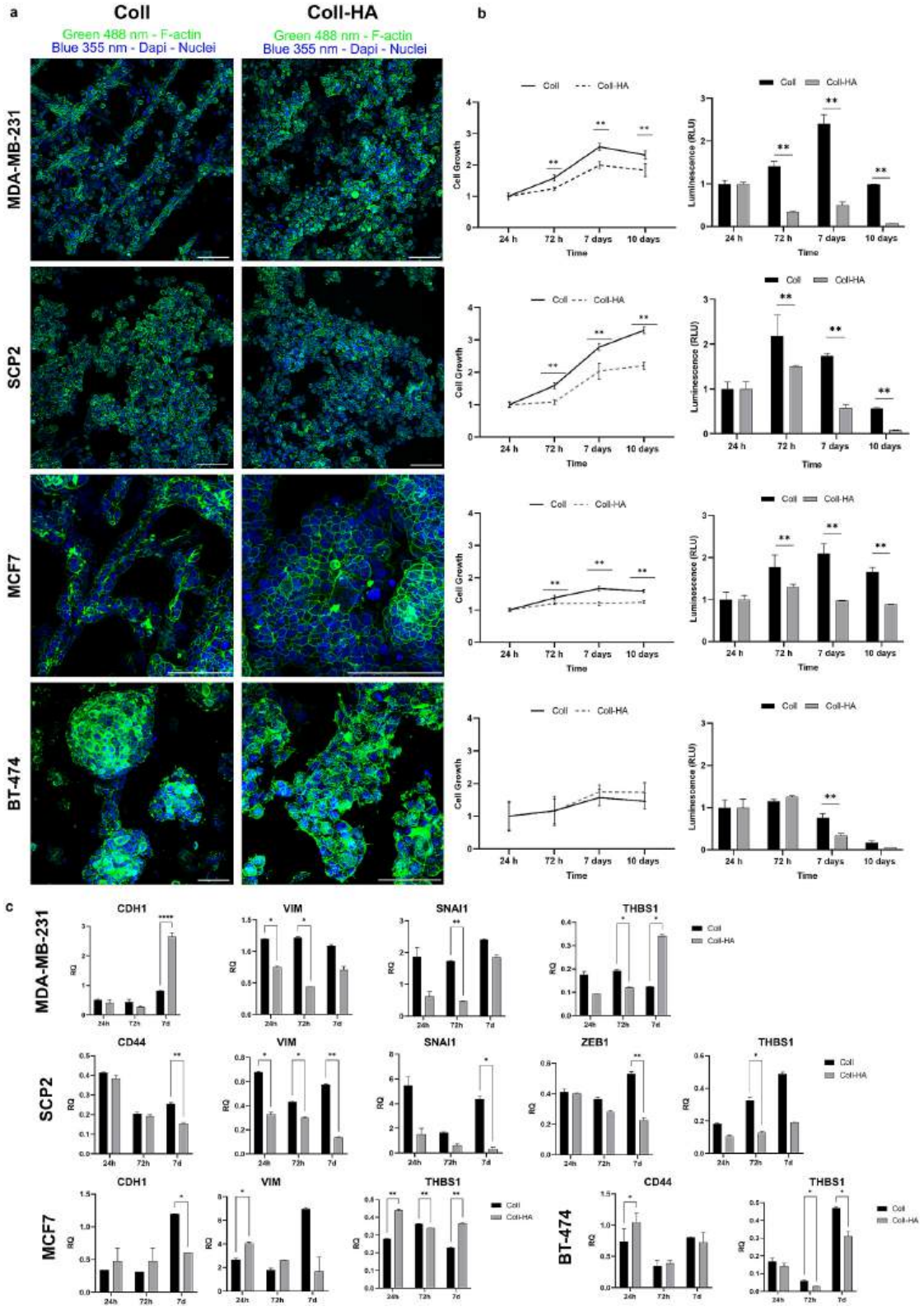

Fig. 2. Breast cancer cell behavior in the coll-HA scaffold. (a) Immunofluorescence images of MDA-MB-231, SCP2, MCF7 and BT-474 cells cultured on the 3D coll and 3D coll-HA models. F-actin is stained in green (488 nm), and nuclei are stained with Dapi (blue, 355 nm). Scale bar = 100 μm. (b) Cell growth analysis over time (24 h, 72 h, 7 days, and 10 days) for MDA-MB-231, SCP2, MCF7 and BT-474 cells cultured on 3D coll (solid line) and the 3D coll-HA scaffold (dashed line); metabolically active cells normalized to the 24 h time point under the same conditions. Statistical significance ($n = 3$): $^{**}P < 0.01$, Error bars show standard deviation (SD). (c) Gene expression analysis (relative quantification, RQ) of epithelial-mesenchymal transition (EMT)-related markers (CDH1, VIM, ZEB1, ZEB2, SNAI1, SNAI2, TJP1, THBS1) in MDA-MB-231, SCP2, MCF7 and BT-474 cells cultured in 3D coll and coll-HA model at different time points (24 h, 72 h, and 7 days). Expression levels in monolayer cultures at the same time point were used as calibrators. Statistical analysis was performed using one-way ANOVA followed by Tukey's post hoc test. Statistical significance ($n = 3$): is indicated as $^{*}P < 0.05$, $^{**}P < 0.01$, $^{***}P < 0.001$, $^{****}P < 0.0001$. Error bars show standard deviation (SD).

= 0.0125 at 72 h), SNAI1 ($P = 0.0148$ at 7 days), ZEB1 ($P = 0.0075$ at 7 days), and THBS1 ($P = 0.0304$ at 72 h), suggesting for SCP2 cells a plasticity toward an epithelial phenotype (Fig. 2c). Analysis of TFs-dependent gene expression revealed a combination of pro-stemness signals associated with TCF12, TCF7L2 and POU5F1, together with induction of epithelial-associated HBP1 and suppression of MYC- and HIF-1α–dependent transcriptional programs (Fig. S3a). Interestingly, MCF7 cells, which already exhibit an epithelial phenotype, show a significant increase in VIM ($P = 0.0351$ at 7 days) and THBS1 ($P = 0.0037$ at 24 h, $P = 0.0074$ at 72 h and $P = 0.0059$ at 7 days), and the loss of expression of CDH1 ($P = 0.012$ at 7 days), consistent with an EMT shift (Fig. 2c). This suggests that while MDA-MB-231 and SCP2 may be partially acquiring epithelial features, MCF7 is transitioning toward a more mesenchymal phenotype. Analysis of TFs-dependent gene expression in MCF7 indicated activation of ZNF263, a promoter of EMT (Fig. S3a). Finally, BT-474 showed an increase in CD44 expression ($P = 0.047$ at 24 h) and a decrease in THBS1 ($P = 0.0152$ at 72 h and $P = 0.019$ at 7 days), while the other analyzed markers showed no significant changes (Fig. 2c). Analysis of TFs-dependent gene expression showed increased stemness and aggressiveness programs associated with TCF3, TFAP2C and E2F4, with concomitant repression of the EMT suppressor ZNF639 (Fig.S3a). Collectively, these data indicate that the ECM modulates the growth dynamics of breast cancer cells and influences their plasticity, inducing subtype-specific EMT or MET shift. Comparison of expression profiles across the different cell lines cultured in coll-HA showed that cell line specific programs remained the dominant determinant of gene expression. The heatmap primarily segregated cell lines according to intrinsic transcriptional identity, distinguishing luminal/epithelial cells (MCF7, BT-474) with enriched estrogen response and apical junction pathways, from mesenchymal/invasive (MDA-MB-231, SCP2) with enriched IL-2/STAT5, TNF-α via NF-kB, EMT and KRAS signalings (Fig. S3b).

Model validity in recapitulating molecular features of bone metastasis was assessed using patient-derived primary specimens. Expression of selected markers, as well as RANK and OPG, key regulators of bone remodeling, were compared between primary bone metastasis and breast cancer cell lines of the corresponding subtype cultured in 3D coll or coll-HA scaffolds. The analysis included three luminal A, one luminal B, and one triple-negative breast cancer bone metastasis specimens. Heatmap cluster analysis revealed that gene expression profiles in coll-HA scaffolds more closely matched those of primary specimens compared with coll scaffolds, with the exception of MDA-MB-231 cells (Fig. S3c). Overall, trends of expression were similar between cells in the scaffold models and primary specimens. The closest correspondence was observed for MCF7 and SCP2. Conversely, MDA-MB-231 showed marked differences compared with the matched primary sample, with some markers being downregulated in the tumor specimens but upregulated in the scaffolds, or vice versa.

2.3. *Bone ECM induces lineage-specific molecular modulations related to metabolic programs and pathways related to bone metastasis*

ECM-induced molecular alterations were determined through RNA sequencing analysis, comparing gene expression of breast cancer cells exposed to coll or coll-HA matrices. A clear separation was observed between the two conditions for all cell lines. Differential gene expression (DE) analysis revealed significantly upregulated and downregulated genes, visualized in the volcano plot and summarized in the accompanying table (Figs. 3b, 4b, 5b, 6b). We used EnrichR [30–32] or GSEA [33] to perform a gene set enrichment analysis to evaluate deregulated pathways, leveraging the MSigDB Hallmark 2020, KEGG and Reactome gene set library database. Significant alterations in metabolic pathways were observed across the different ECM conditions. When cultured in coll-HA scaffolds, MDA-MB-231 cells downregulated genes related to the ribosome pathway (NES -1.85, padj = 0.01) and other protein-synthesis related pathways such as translation (NES -1.91, padj = 0.03) (Fig. 3c). This suggests an adaptive response aimed at conserving energy by reducing protein synthesis, aligning with the observed reduction in proliferation. The SCP2 cell line similarly showed downregulation of the ribosome pathway (NES -2.63, padj <0.05) and of two other metabolic pathways: the metabolism of aminoacids and derivatives (NES -2.42, padj <0.05) and the selenoamino acid metabolism (NES -2.52, padj <0.05) (Fig. 4c). MCF7 cells cultured in coll-HA scaffolds demonstrated upregulation of lipid metabolism (NES 1.79, padj <0.05), aerobic respiration and the respiratory electron transport chain (NES 2.479, padj <0.05), alongside downregulation of aminoacids and derivatives metabolism (NES -2.31, padj <0.05), selenoaminoacids metabolisms (NES -2.59, padj <0.05) and the ribosome pathway (NES -2.58, padj <0.05), the last consistent with the other cell lines (Fig. 5c). These findings suggest that exposure to bone-mimetic environments may be associated with a common response involving reduced protein biosynthesis, together with lineage-specific metabolic changes that may contribute to differences in cancer cell adaptation [34–36]. Pathways implicated in bone metastasis were also modulated. In MDA-MB-231 cells there was upregulation of IL2/STAT5 signaling (odds ratio 7.44; $P = 0.03$), apical junction (odds ratio 7.49; $P = 0.03$), EMT (odds ratio 7.40; $P = 0.03$) and Hedgehog signaling (odds ratio 20.34; $P = 0.051$) (Fig. 3c). In SCP2 cells, axon guidance pathways, associated with Ephrin and Semaphorin signaling [37], which support metastatic cell survival and colonization, were upregulated (Fig. 4c). MCF7 cells showed increased activity in the MAPK signaling cascade (Fig. 5c). Notably, all the three cell lines demonstrated significant downregulation of the SLIT/ROBO signaling axis, which plays a key role in bone homeostasis by inhibiting osteoclastogenesis and promoting osteoblast function [38]. No significantly altered pathways were detected in BT-474, further underscoring the limited adaptive response of this cell line to the bone-mimetic environment. Moreover, to focus on transcriptional programs involved in the communication between tumor cells and their surrounding microenvironment, we investigated Gene Ontology Biological Process (GO-BP) pathways associated with ECM interaction, organization, and related cellular signaling mechanisms (Fig. S4). No significant differences were observed between coll and coll-HA scaffolds in any of the analyzed cell lines. However, comparing exposure to coll or coll-HA scaffolds with two dimensional (2D) cultures revealed marked and cell-type-specific transcriptional responses. MDA-MB-231 showed a reduction of ECM-interaction programs in 3D cultures, with coll–HA scaffolds inducing downregulation of extracellular matrix organization (NES -1.91, padj 9.72×10^{-3}) and cell–matrix adhesion (NES -1.53, padj 1.80×10^{-2}), and with coll scaffolds similarly reducing cell–matrix adhesion (NES -1.49, padj 3.12×10^{-2}). SCP2 cells displayed a distinct response characterized by activation of cytoskeletal remodeling programs in both 3D cultures. Coll-HA scaffolds promoted regulation of cytoskeleton organization (NES 1.39, padj 2.38×10^{-2}), while reducing regulation of extracellular matrix disassembly (NES -1.87, padj 2.57×10^{-2}). Similarly, coll scaffolds induced regulation of cytoskeleton organization (NES 1.36, padj 2.63×10^{-2}) and actin filament organization (NES 1.35, padj 3.70×10^{-2}). BT-474 cells exhibited a strong ECM-engaged phenotype in both coll and coll-HA scaffolds, characterized by enrichment of collagen remodeling, matrix assembly, and adhesion-related programs. Coll-HA scaffolds induced enrichment of collagen fibril organization (NES 2.01, padj 1.28×10^{-3}), cell–matrix adhesion (NES 1.60, padj 3.51×10^{-3}), extracellular matrix assembly (NES 1.90, padj 1.06×10^{-2}), extracellular matrix disassembly (NES 1.66, padj 3.46×10^{-2}), positive regulation of extracellular matrix organization (NES 1.81, padj 3.10×10^{-2}), positive regulation of cell–matrix adhesion (NES 1.64, padj 3.46×10^{-2}), while reducing cytoskeleton organization (NES -1.19, padj 3.46×10^{-2}). Similarly, coll scaffolds induced significant enrichment of extracellular matrix assembly (NES 2.20, padj 1.62×10^{-4}), extracellular matrix disassembly (NES 1.69, padj 2.75×10^{-2}), collagen fibril organization (NES 2.06, padj 1.62×10^{-4}), cell–matrix adhesion NES 1.73, padj 1.62×10^{-4}), and regulation of extracellular matrix organization (NES 1.60, padj 2.75×10^{-2}). Conversely, MCF7 cells did not exhibit significant transcriptional changes in the analyzed

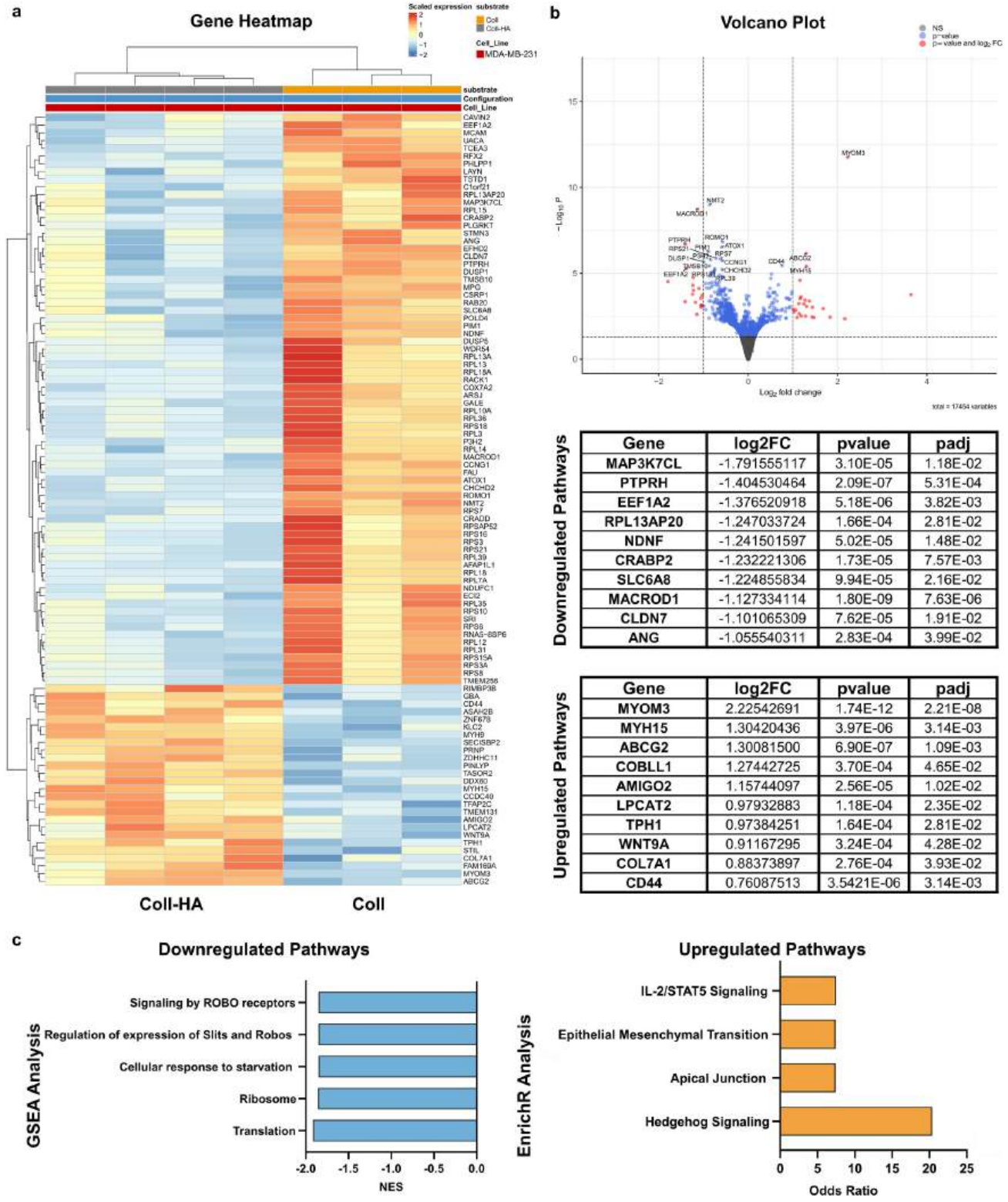

Fig. 3. RNA sequencing analysis of MDA-MB-231 cells cultured in coll and coll-HA scaffold. (a) Gene expression heatmap: Differential gene expression between coll and coll-HA substrates. Colors represent scaled gene expression, with red indicating significant upregulated genes and blue indicating downregulated genes. (b) Volcano plot of differentially expressed genes (DEGs): The plot visualizes statistical significance (Y-axis, −log10 *P*-value) versus fold change in expression (X-axis, log2 fold change). Red dots indicate significantly differentially expressed genes (p-adj < 0.05). A table highlights the most upregulated and downregulated genes. (c) Pathway enrichment analysis: Bar plots show the most affected biological processes and pathways. On the left, downregulated pathways were identified by GSEA analysis and include signaling related to Slit and Robo receptors, ribosome pathway, translation pathway and cellular response to starvation. On the right, upregulated pathways were identified by EnrichR analysis and include the IL2/STAT5 signaling pathway, EMT, apical junction and Hedgehog signaling. Statistical significance: *P*-value<0.05 or *p-adj < 0.05.

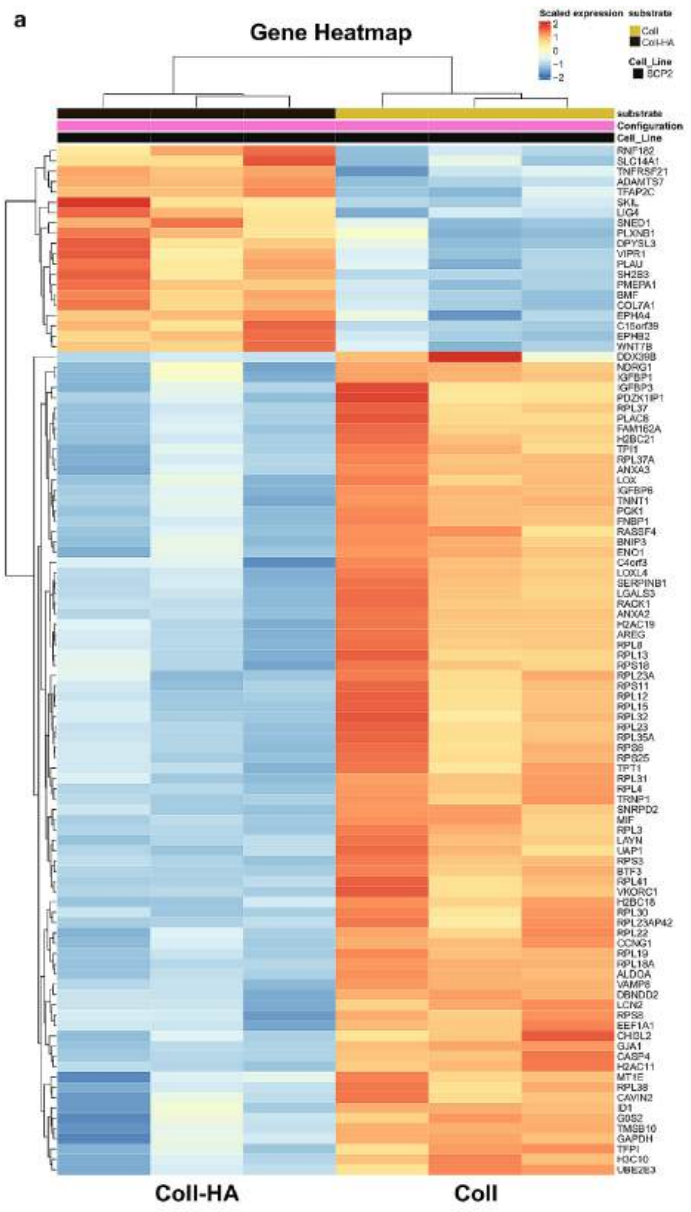

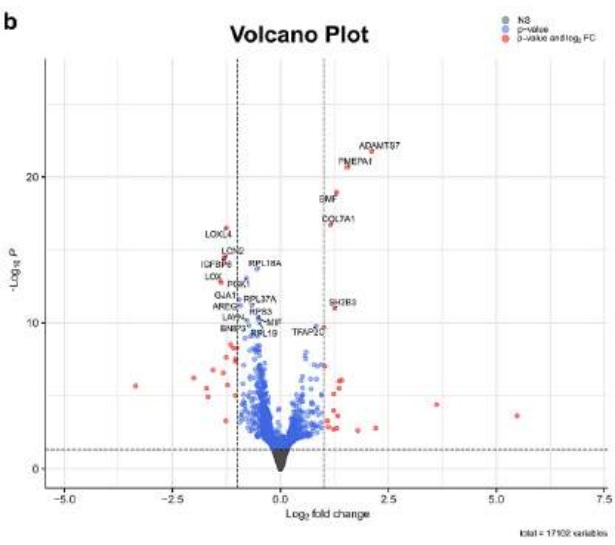

Downregulated Pathways

Gene	log2FC	pvalue	padj
ADAMTS7	2.111104	1.78E-22	2.10E-18
PMEPA1	1.551578	2.17E-21	1.28E-17
SLC14A1	1.418679	8.79E-07	1.14E-04
PLXNB1	1.359427	9.90E-07	1.26E-04
AMIGO2	1.357764	3.01E-06	2.93E-04
IL24	1.331704	2.34E-04	9.02E-03
FOSB	1.304881	1.70E-03	3.85E-02
BMF	1.299696	1.18E-19	4.66E-16
SH2B3	1.254339	1.00E-11	8.44E-09
HMCN1	1.235717	7.68E-06	6.57E-04

Upregulated Pathways

Gene	log2FC	pvalue	padj
EID1	-1.71455	2.92E-06	2.87E-04
LOX	-1.37273	1.71E-13	2.01E-10
TRNP1	-1.32385	2.61E-07	4.22E-05
IGFBP6	-1.30671	3.87E-15	6.52E-12
LCN2	-1.29064	3.09E-15	6.07E-12
PDZK1IP1	-1.25613	2.32E-08	5.71E-06
LOXL4	-1.24872	3.12E-17	7.37E-14
APLN	-1.22119	1.83E-06	2.04E-04
IGFBP3	-1.14885	3.02E-09	1.19E-06
G0S2	-1.09036	5.30E-09	1.79E-06

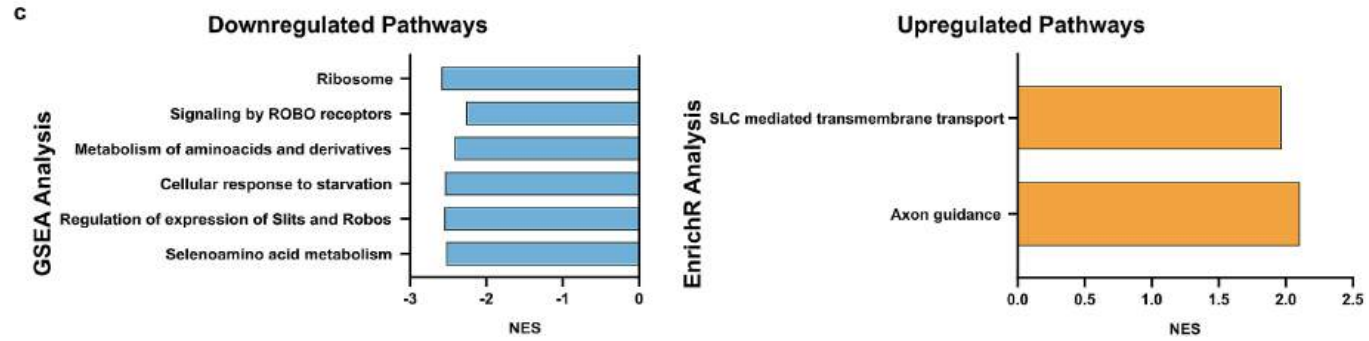

Fig. 4. RNA sequencing analysis of SCP2 cells cultured in coll and coll-HA scaffold. (a) Gene expression heatmap: Differential gene expression between coll and coll-HA substrates. Colors represent scaled gene expression, with red indicating significant upregulated genes and blue indicating downregulated genes. (b) Volcano plot of differentially expressed genes (DEGs): The plot visualizes statistical significance (Y-axis, −log10 *P*-value) versus fold change in expression (X-axis, log2 fold change). Red dots indicate significantly differentially expressed genes. A table highlights the most upregulated and downregulated genes. (c) Pathway enrichment analysis: Bar plots show the most affected biological processes and pathways analyzed with GSEA. On the left, downregulated pathways include ribosome, cellular response to starvation, regulation of expression of Slits and Robo pathways. On the right, upregulated pathways include the SLC mediated transmembrane transport and the axon guidance pathway.

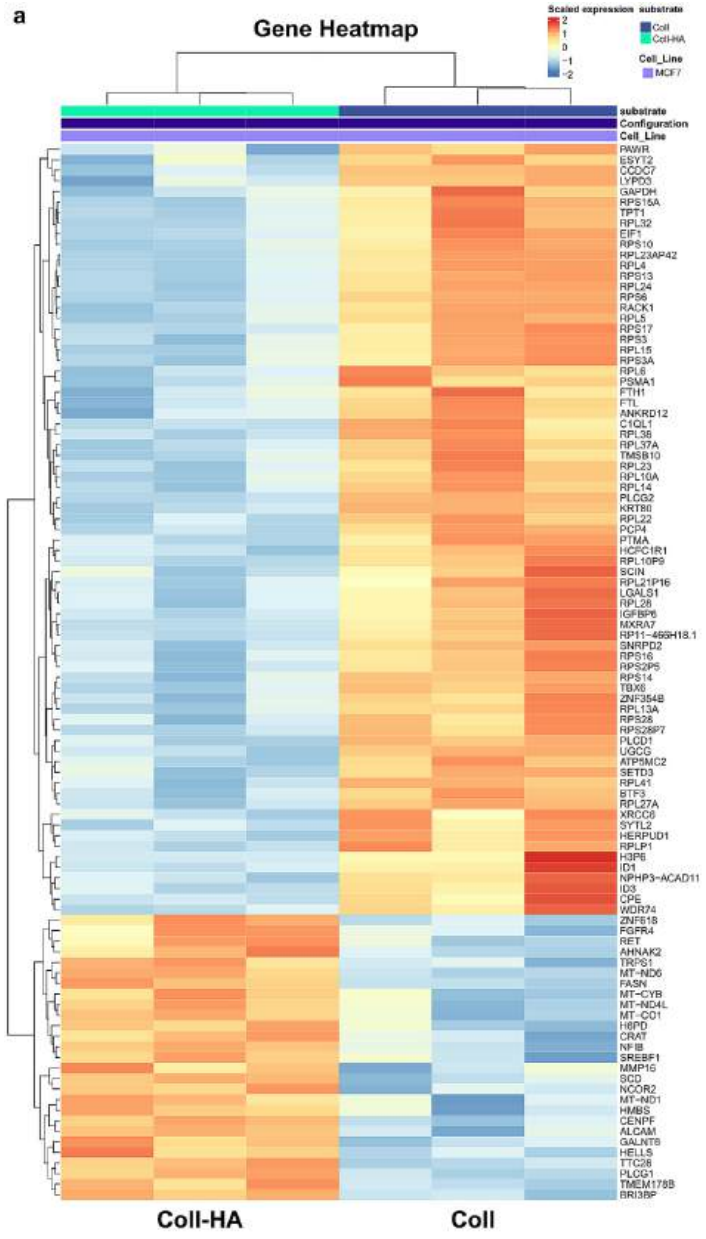

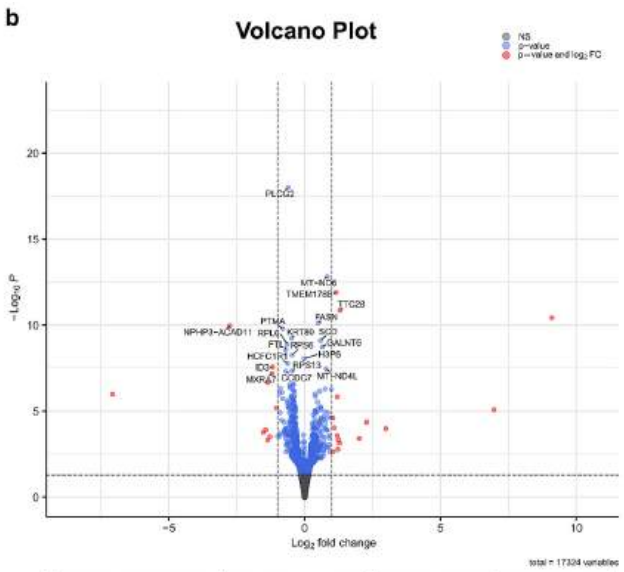

Downregulated Pathways

Gene	log2FC	pvalue	padj
TTC28	1.303201	1.35E-11	4.04E-08
CRAT	1.195483	1.45E-06	4.29E-04
PHRF1	1.189045	2.58E-04	1.52E-02
TMEM178B	1.154133	1.23E-12	4.90E-09
GGT1	1.090464	9.42E-05	7.61E-03
AFF3	1.029113	2.59E-05	2.97E-03
RET	0.984482	5.50E-07	2.23E-04
PCDH19	0.960861	2.51E-05	2.94E-03
TAP1	0.913348	2.56E-04	1.52E-02
MAPK4	0.898577	3.54E-04	1.81E-02

Upregulated Pathways

Gene	log2FC	pvalue	padj
NPHP3	-2.76245	1.11E-10	2.20E-07
ID1	-1.35937	2.16E-07	1.23E-04
CALB2	-1.3557	4.65E-04	2.20E-02
MXRA7	-1.19928	6.32E-08	3.78E-05
ID3	-1.18015	2.67E-08	1.99E-05
IGFBP6	-1.03423	6.38E-06	1.16E-03
KCNF1	-0.99014	2.88E-04	1.60E-02
TBX6	-0.93778	8.88E-07	3.03E-04
GFRA2	-0.93151	2.02E-04	1.31E-02
DDAH2	-0.93082	2.92E-04	1.61E-02

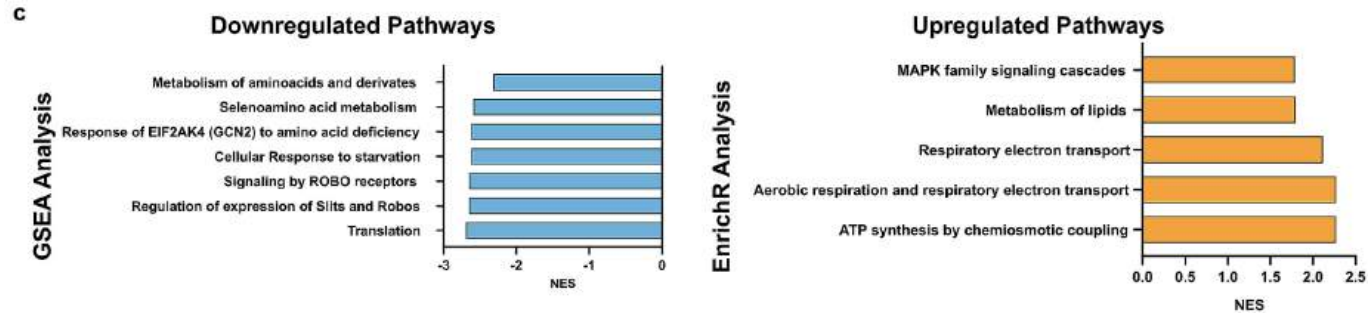

Fig. 5. RNA sequencing analysis of MCF7 cells cultured in coll and coll-HA scaffold. (a) Gene expression heatmap: Differential gene expression between coll and coll-HA substrates. Colors represent scaled gene expression, with red indicating significant upregulated genes and blue indicating downregulated genes. (b) Volcano plot of differentially expressed genes (DEGs): The plot visualizes statistical significance (Y-axis, −log10 *P*-value) versus fold change in expression (X-axis, log2 fold change). Red dots indicate significantly differentially expressed genes. A table highlights the most upregulated and downregulated genes. (c) Pathway enrichment analysis: Bar plots show the most affected biological processes and pathways, analyzed with GSEA. On the left, downregulated pathways include translation pathway, ribosome, regulation of expression of Slits and Robo, cellular response to starvation pathways. On the right, upregulated pathways include MAPK family signaling cascades, the metabolism of lipids pathway, the respiratory electron transport, the aerobic respiration, and respiratory electron transport pathway.

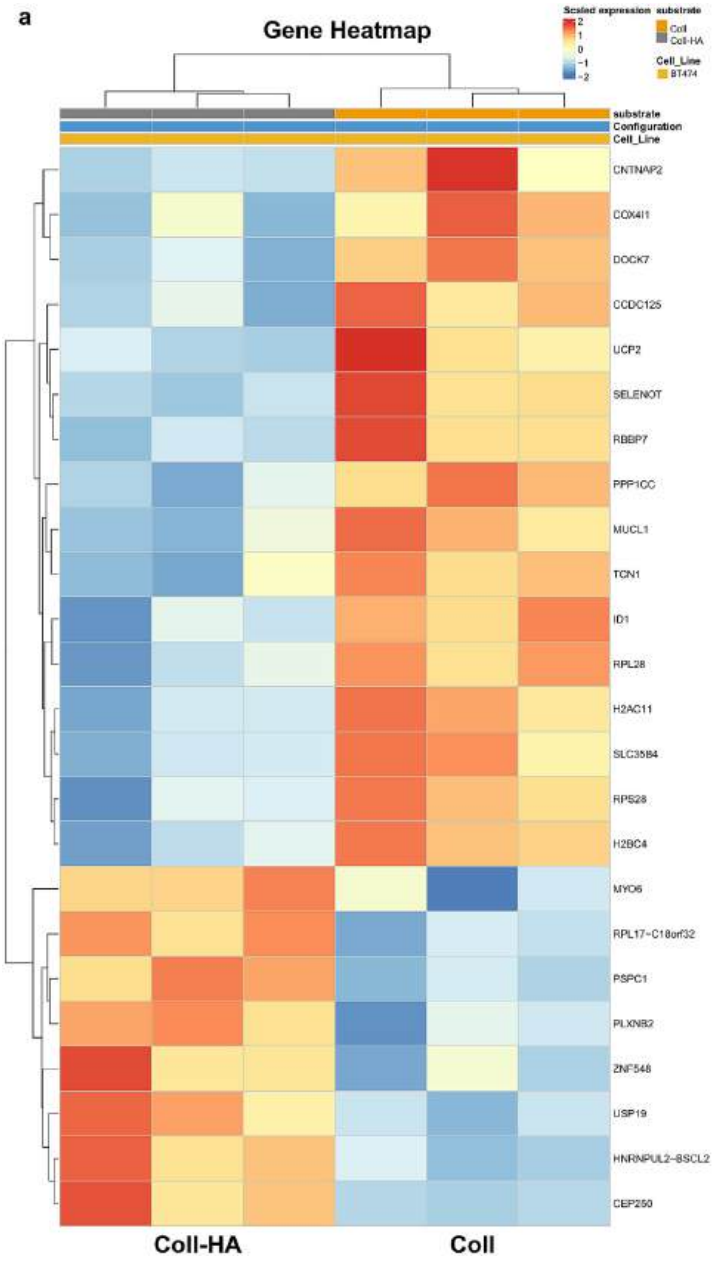

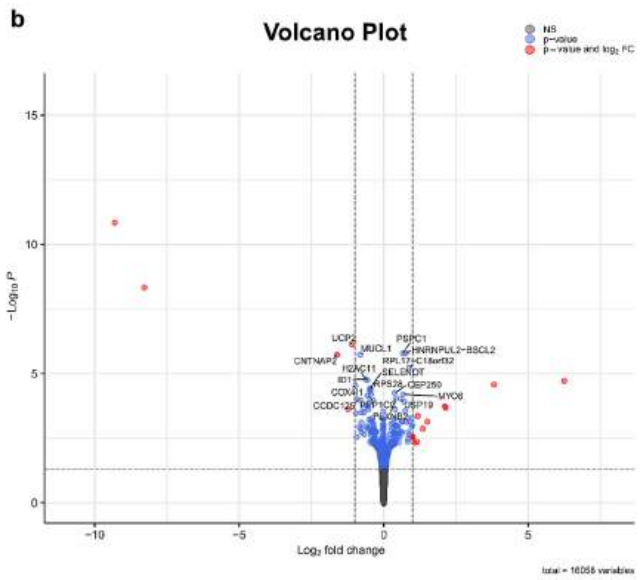

Downregulated Pathways

Gene	log2FC	pvalue	padj
RPL17-C18orf32	0.886282	0.0000058	0.008893
HNRNPUL2-BSCL2	0.761588	0.00000162	0.003402
ZNF548	0.71514	0.000124	0.049023
MYO6	0.663226	0.0000628	0.036213
PSPC1	0.656269	0.00000164	0.003402
USP19	0.596361	0.0000942	0.045374
PLXNB2	0.423558	0.0000913	0.045374
CEP250	0.388075	5.41E-05	3.56E-02

Upregulated Pathways

Gene	log2FC	pvalue	padj
CNTNAP2	-1.60924	1.83E-06	3.40E-03
UCP2	-1.09017	7.41E-07	3.40E-03
COX4I1	-0.97284	2.91E-05	2.97E-02
CCDC125	-0.92848	9.86E-05	4.54E-02
SLC35B4	-0.81188	1.07E-04	4.67E-02
MUCL1	-0.81125	1.85E-06	3.40E-03
ID1	-0.62357	1.63E-05	2.09E-02
H2AC11	-0.56667	1.82E-05	2.09E-02
PPP1CC	-0.5635	7.18E-05	3.88E-02
TCN1	-0.50663	1.28E-04	4.90E-02

Fig. 6. RNA sequencing analysis of BT-474 cells cultured in coll and coll-HA scaffold. (a) Gene expression heatmap: Differential gene expression between coll and coll-HA substrates. Colors represent scaled gene expression, with red indicating significant upregulated genes and blue indicating downregulated genes. (b) Volcano plot of differentially expressed genes (DEGs): The plot visualizes statistical significance (Y-axis, −log10 *P*-value) versus fold change in expression (X-axis, log2 fold change). Red dots indicate significantly differentially expressed genes. A table highlights the most upregulated and downregulated genes.

ECM-related pathways following transition from 2D to 3D culture. Overall, these findings indicate that, while the presence of mineralization has a negligible impact, exposure to 3D culture conditions induces subtype-dependent transcriptional reprogramming of matrix interaction pathways and ECM organization programs.

2.4. ECM modulates sensitivity of breast cancer cells to bone targeted drugs

We next examined whether different ECMs modulate breast cancer cell sensitivity to bone-targeted drugs. Cells were treated with Zoledronic Acid (Zol, ZOMETA®) and Denosumab (Deno, an anti-RANKL inhibitor) at their respective plasma peak concentrations. Compared the respective untreated condition, MDA-MB-231 cells cultured in the coll-HA scaffold exhibited 98% survival following Deno treatment (P = ns) and 92% survival following Zol treatment ($P = 0.002$), while survival in 2D and in coll scaffolds was not affected, as these cells are intrinsically insensitive to both drugs (Fig. 7a). The osteotropic subclone SCP2 displayed an intrinsic sensitiveness to Zol in 2D (77% survival compared the respective no-treated condition, $P = 0.004$), which was confirmed in coll-HA scaffold (85% survival, $P = 0.0004$), whereas they showed reduced sensitivity to treatment when cultured in coll scaffold (95% survival, P = ns) (Fig. 7b). Interestingly, SCP2 cells exhibited significant sensitivity to Deno treatment when cultured in coll-HA scaffolds, with a survival rate of 70% ($P < 0.0001$). In contrast, Deno treatment showed minimal efficacy in 2D and coll scaffold, with survival rates of 95% (P = ns) and 93% ($P = 0.01$), respectively, compared to their untreated controls. A similar result was observed for MCF7 cells that, when cultured in the coll-HA scaffold, demonstrated a significant increase in sensitivity to both drugs, with survival rates of 85% ($P = 0.0001$)

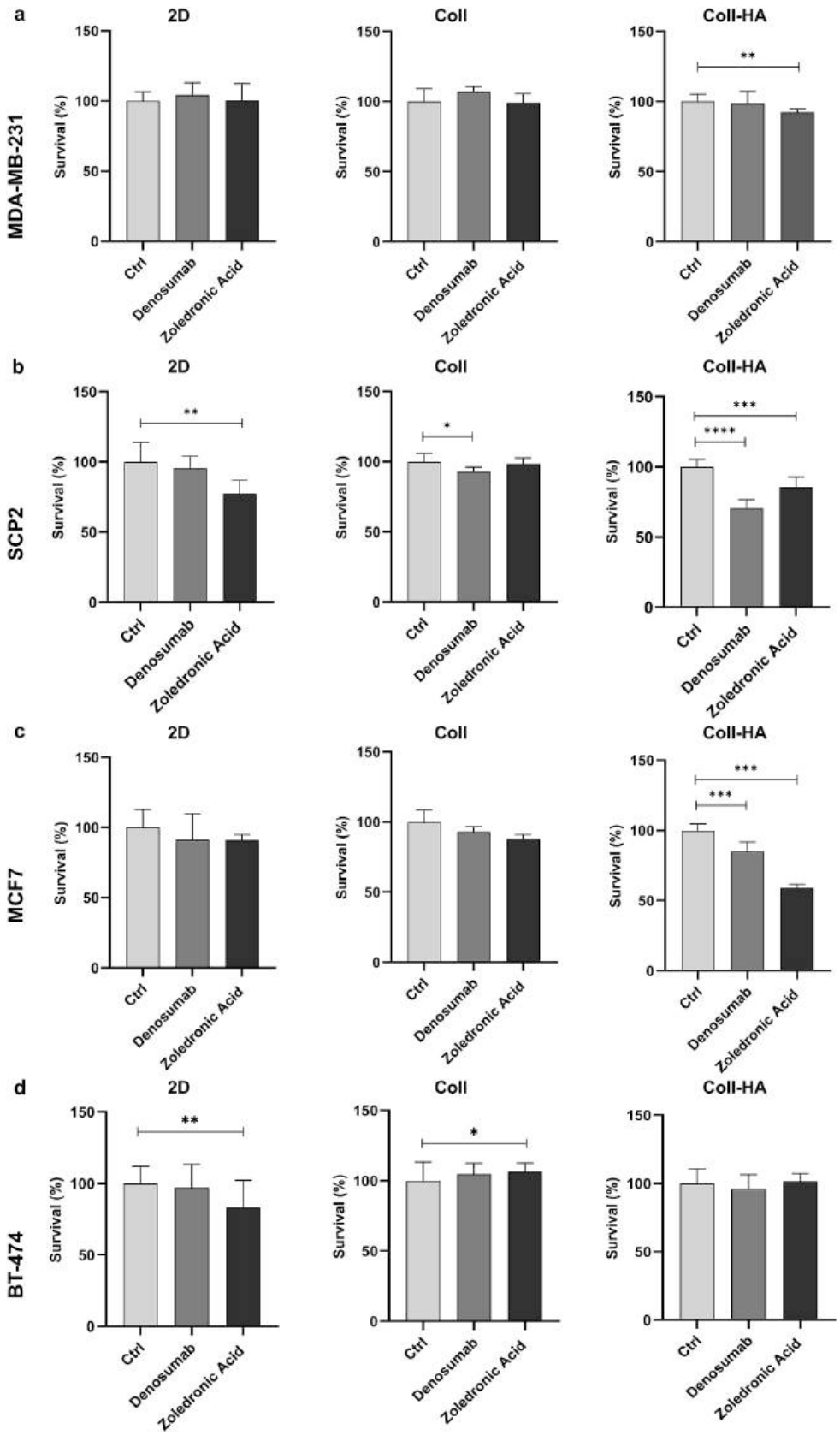

Fig. 7. Effects of Bone Targeted Drugs (Denosumab and Zoledronic Acid) on Breast Cancer Cell Survival in Different Culture Conditions. Bar graphs represent the survival percentage to treatment under different culture conditions (2D, 3D coll, and 3D coll-HA scaffold). (a) MDA-MB-231 cell line survival; (b) SCP2 cell line survival; (c) MCF7 cell line survival; (d) BT-474 cell line survival. Statistical significance (n = 3): $^{*}P < 0.05$, $^{**}P < 0.01$, $^{***}P < 0.001$, $^{****}P < 0.0001$. Error bars show standard deviation (SD).

following Deno treatment and 59% ($P < 0.00001$) following Zol treatment (Fig. 7c). Conversely, this cell line exhibited low intrinsic sensitivity to both Deno and Zol in 2D culture (survival percentage: 91%, $P =$ ns and 90%, $P =$ ns, respectively), with no significant change in the coll model (92% survival, $P =$ ns and 87% survival, $P = 0.005$ survival). BT-474 cells were refractory to both treatments, with the exception of Zol, which exhibited modest yet statistically significant activity when administered in 2D cultures ($P = 0.0054$). Notably, BT-474 cells displayed increased resistance to Zol when cultured in coll scaffolds ($P = 0.0323$) (Fig. 7d).

To further investigate the response to Denosumab, we analyzed protein expression of RANK and RANKL in breast cancer cells cultured in 2D or within 3D scaffolds. 3D culturing resulted in a marked increase in RANKL expression compared to monolayer cultures in all cell lines, with the highest RANKL levels detected in the coll-HA scaffolds (Fig. S5c). Quantification of fluorescence intensity showed an upregulation of RANKL in 3D scaffolds, particularly in the coll-HA matrix ($P < 0.0001$ for all four cell lines) (Fig. S5b). These findings may provide a potential mechanistic explanation for the increased sensitivity to Deno observed in the coll-HA scaffolds. RANK protein was not detected in any of the cell lines (data not shown).

2.5. ECM-breast cancer cell interactions influence osteoclast differentiation

To evaluate the influence of the different ECM conditions on osteoclastogenic potential, we examined the ability of conditioned medium (CM) containing soluble factors secreted by breast cancer cells cultured in 2D, coll, and coll-HA scaffolds to induce osteoclast differentiation from PBMCs (Fig. 8). Factors secreted by ER- cell lines, MDA-MB-231 and SCP2, similarly promoted osteoclastogenesis. The mean number (n°) of osteoclasts (OC) per field induced by MDA-MB-231 cultured in coll scaffolds was 76.2, while it was 80.7 when cultured in coll-HA scaffolds (Fig. 8b). These values were significantly higher than the 47 OCs/field observed when MDA-MB-231 cells were cultured in the 2D condition ($P = 0.0007$ and $P = 0.0001$, respectively), while no significant difference was observed between the two scaffolds. Compared the positive control (Ctrl+), in which differentiation was induced only by M-CSF and RANKL (32.63 OCs/field), osteoclastogenesis was significantly increased in both coll and coll-HA scaffolds ($P < 0.0001$for both comparisons), but not when cultured in 2D.

Similarly, SCP2 cells, induced a significantly higher number of osteoclasts when cultured in coll (86.25 OCs/field) or coll-HA scaffolds (91.13 OCs/field), compared to 2D culture (60.13 OCs/field) ($P = 0.0002$ and $P < 0.0001$, respectively). Again, no significant difference was found between the two scaffolds. Compared to the Ctrl+, all three SCP2-derived conditions showed significantly increased osteoclastogenesis ($P < 0.0001$ for all comparisons) (Fig. 8b).

In contrast, the luminal A breast cancer cell line MCF7 exhibited limited osteoclastogenic activity when cultured in 2D, with only 14.9 OCs/field, significantly lower than the Ctrl+ (32.6 OCs/field, $P = 0.0152$). However, when MCF7 cells were cultured in 3D, osteoclastogenesis was markedly enhanced: 67.5 OCs/field in coll scaffold and 84.4 OCs/field in coll-HA scaffold. These increases were statistically significant both compared to the Ctrl+ ($P < 0.0001$ for both scaffolds) and to 2D conditions ($P < 0.0001$ for both). Additionally, the difference between coll and coll-HA scaffolds was also significant ($P = 0.0129$) (Fig. 8b).

In contrast, BT-474 cells cultured both in 2D and 3D conditions did not show the capability to induce osteoclast differentiation (Fig. S5a).

To investigate which soluble factor correlates with the increased osteoclastogenic potential observed in the coll and coll-HA scaffolds, we analyzed the secretion of TNF-α, IL-6, and IL-8, inflammatory cytokines that mediates monocyte-to-osteoclast differentiation (Fig. 8c). Cytokine expression patterns differed across breast cancer subtypes when comparing 3D scaffolds (coll and coll-HA) to 2D cultures. A consistent upregulation of TNF-α was observed in both 3D conditions for MDA-MB-231 and MCF7 cells. Specifically, TNF-α levels significantly increased, compared to 2D culture, in coll ($P = 0.0108$ for MDA-MB-231 and $P = 0.00132$ for MCF7) and were further elevated in coll-HA scaffolds ($P < 0.0001$ for MDA-MB-231 and $P = 0.0052$ for MCF7). In MDA-MB-231, TNF-α levels significantly increased in coll-HA scaffolds compared with coll scaffolds ($P < 0.0001$). In contrast, SCP2 cells showed a significant reduction in TNF-α secretion in coll scaffolds compared to 2D ($P = 0.006$), while no significant difference was observed in coll-HA scaffolds. IL-6 and IL-8 expression showed a lineage- and matrix-specific modulation. In both 3D conditions, compared to 2D, SCP2 cells exhibited a robust upregulation of IL-6 ($P = 0.0008$ for coll and $P < 0.0001$ for coll-HA) and IL-8 ($P < 0.0001$ for both). The increase in IL-6 was significantly higher in coll-HA scaffolds compared with coll scaffolds, whereas the opposite trend was observed for IL-8 ($P = 0.001$ for IL-6 and $P = 0.0004$ for IL-8). Similarly, MCF7 cells upregulated IL-6 in coll-HA scaffolds ($P = 0.0041$) and IL-8 in both coll ($P = 0.0002$) and coll-HA conditions ($P = 0.0005$). Conversely, MDA-MB-231 cells displayed a distinct response. Despite the upregulation of TNF-α, both IL-6 and IL-8 were significantly downregulated in coll-HA scaffolds compared to 2D ($P < 0.0001$for both), while IL-8 was significantly increased in coll scaffold ($P < 0.0001$). Both cytokines were significantly downregulated in the coll-HA scaffolds relative to the coll scaffolds ($P < 0.0001$for both comparisons).

Overall, these findings highlight that the 3D microenvironment may differentially modulate inflammatory signaling in a lineage-specific manner. IL-6 and IL-8 are generally upregulated in bone-tropic SCP2 and epithelial-like cell line MCF7, while TNF-α expression appears upregulated in MDA-MB-231 and MCF7 cells (Fig. 8c).

2.6. ECM-Breast cancer cell interactions modulate osteoclast sensitivity to bone-targeted therapies

We next investigated whether tumor-derived cytokines influence osteoclast sensitivity to bone-targeted agents Deno and Zol (Fig. 8d). To assess this, we employed an indirect co-culture system in which osteoclast precursors were treated with CM collected from MDA-MB-231, SCP2, or MCF7 breast cancer cells cultured in 2D and 3D models (Fig. S6b). Osteoclast precursors exposed to CM from MDA-MB-231 cells cultured in coll-HA scaffolds exhibited significantly increased sensitivity to Deno compared to those treated with CM from 2D ($P = 0.0015$) or coll scaffold cultures ($P = 0.0019$). Notably, MDA-MB-231 cells grown in coll-HA scaffolds showed reduced expression of IL-6 and IL-8 compared to 2D and coll conditions, which may underline this increased drug responsiveness. In contrast, osteoclasts exposed to CM from MDA-MB-231 cells grown in both coll and coll-HA scaffolds showed greater resistance to Zol compared to 2D ($P < 0.0001$ for both conditions) (Fig. 8d). Osteoclasts induced by SCP2 CM from coll-HA scaffolds exhibited increased resistance to both Deno and Zol compared to CM from monolayer culture ($P < 0.0001$ for both conditions). Similarly, SCP2 CM from coll scaffolds also conferred resistance to Deno ($P < 0.0001$) and Zol ($P = 0.0135$) compared to 2D. The resistance to Zol induced by CM from coll-HA scaffolds was significantly higher than that induced by CM from coll scaffolds ($P < 0.0001$) (Fig. 8d). Osteoclasts induced by MCF7 did not show significant changes in responsiveness to Deno depending on the CM used. However, osteoclasts induced by CM from MCF7 cultured in coll-HA scaffolds showed increased resistance to Zol relative to 2D ($P = 0.0052$) (Fig. 8d). Collectively, these findings suggest that tumor cell-ECM interactions contribute to shaping the paracrine environment that regulates osteoclast differentiation and responsiveness to bone-targeted therapies.

3. Discussion

Bone metastasis from breast cancer is a complex process affected not only by the intrinsic genetic properties of cancer cells but also by the

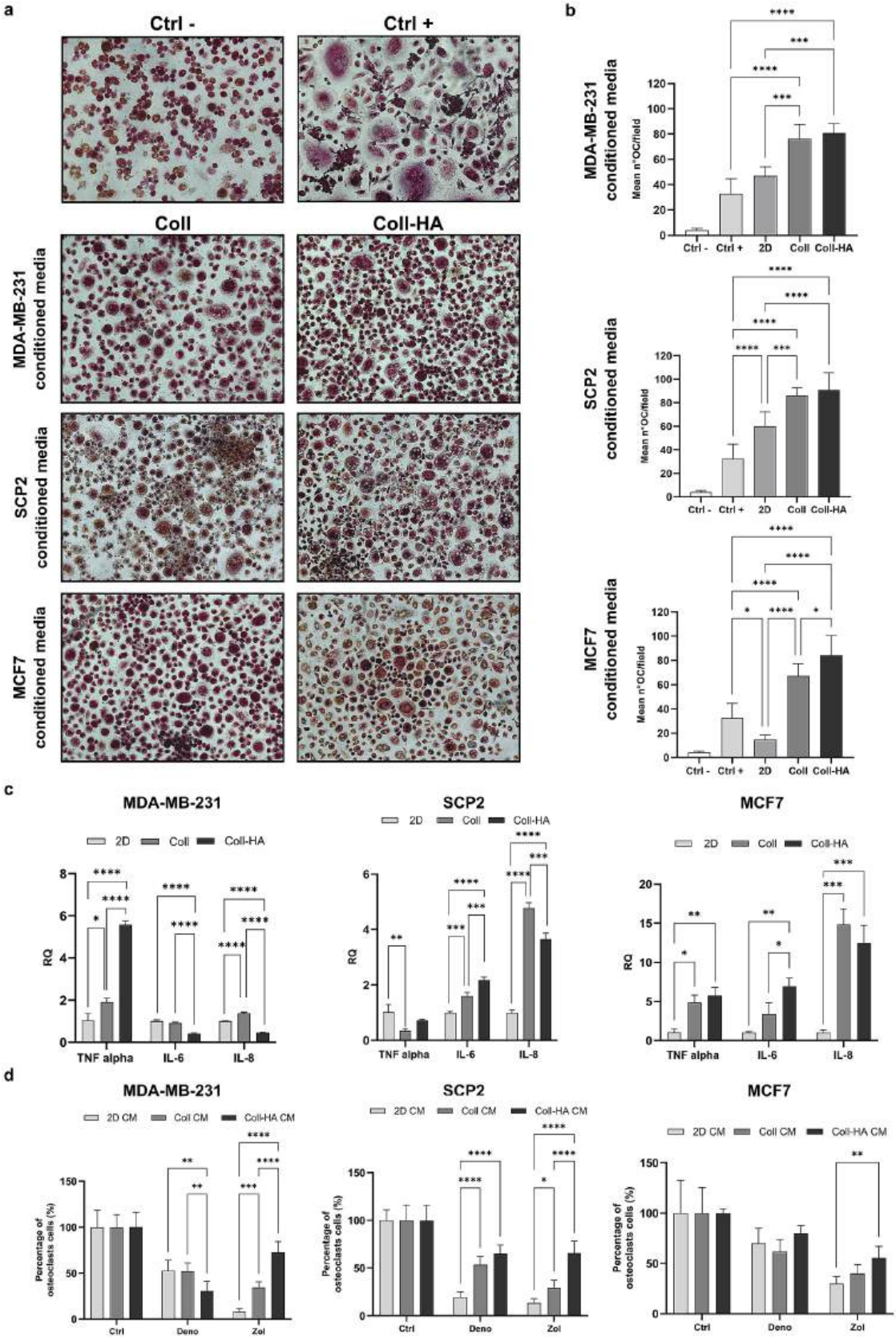

(caption on next page)

Fig. 8. Indirect Co-culture between Breast Cancer Cells and Osteoclasts (differentiated from hPBMCs). (a) Representative pictures for each condition of hPBMCs and differentiated osteoclasts after 15 days of differentiation with M-CSF and RANKL (Ctrl+) or with conditioned medium (CM) from breast cancer cells cultured in 2D or 3D coll or 3D coll-HA. CM was collected at 7 days of culture and added to complete α-MEM to obtain a CM with 20% cancer cell medium and 80% α-MEM. (b) Mean number of osteoclasts/field for each condition (MDA-MB-231, SCP2 and MCF7). Differentiated osteoclasts were identified as cells positive to TRAP staining and with >4 nuclei. Statistical analysis was performed using one-way ANOVA followed by Tukey's post hoc test. For all comparisons, statistical significance ($n = 3$) is indicated as $^{*}P < 0.05$, $^{**}P < 0.01$, $^{***}P < 0.001$, $^{****}P < 0.0001$. Error bars show standard deviation (SD). (c) Gene expression analysis (relative quantification, RQ) of pro-inflammatory cytokines (TNF-α, IL-6, IL-8) in MDA-MB-231, SCP2, and MCF7 cells cultured in different conditions (2D, 3D coll, 3D coll-HA scaffold) at 7 days. Statistical analysis was performed using one-way ANOVA followed by Tukey's post hoc test. For all comparisons, statistical significance ($n = 3$) is indicated as $^{*}P < 0.05$, $^{**}P < 0.01$, $^{***}P < 0.001$, $^{****}P < 0.0001$. Error bars show standard deviation (SD). (d) Osteoclasts survival percentage (%) after Denosumab and Zoledronic Acid treatment. Osteoclasts differentiation was induced by tumor cells CM collected at 7 days of cultures and added to complete α-MEM to obtain a CM with 20% cancer cell medium and 80% α-MEM. Percentage was evaluated compared to the respective no treated control. Statistical analysis was performed using two-way ANOVA followed by Tukey's post hoc test. For all comparisons, statistical significance ($n = 3$) is indicated as $^{*}P < 0.05$, $^{**}P < 0.01$, $^{***}P < 0.001$, $^{****}P < 0.0001$. Error bars show standard deviation (SD).

interaction of disseminated cells with the bone microenvironment [39]. This study underscores the critical role of the "soil", the bone microenvironment, focusing on the surrounding ECM, in guiding breast cancer cell phenotypes and behavior. This reprogramming may involve epigenetic remodeling [40], stemness acquisition [41], and metabolic shifts [42,43], all of which contribute to increased metastatic potential. Modeling these pathological events may enhance our mechanistic understanding of bone metastasis and reveal microenvironment-dependent vulnerabilities. To this aim, we developed and validated a coll-HA scaffold that reproduces key features of the bone ECM, allowing the specific contribution of matrix composition to be explored in a controlled setting. The developed materials exhibited interconnected pores of 20–100 μm that facilitates efficient nutrient and oxygen diffusion while allowing cells to infiltrate throughout the scaffold, thereby overcoming key limitations of dense or poorly interconnected 3D matrices [44]. The scaffolds rapidly absorbed water and retained stable hydration, sustaining cell viability throughout the 3D structure. Together, these physicochemical parameters are critical for the establishment of supportive and relevant microenvironments [45]. Incorporation of HA into collagen enhanced matrix stiffness and promoted intermolecular interactions. These composite materials demonstrated high mechanical stability and long-term structural integrity, enabling to reproduce biomechanical cues that are critical regulators of key breast cancer cell phenotypes such as adhesion, proliferation, invasion and stem-like properties. These effects are not captured in standard 2D cultures or in matrices with suboptimal stiffness [46]. Finally, incorporation of HA also provided a mineralized interface that is capable of directly influencing cancer cell behavior [47].

These materials were challenged with four cell lines, representative of clinically relevant breast cancer subtypes: MDA-MB-231, a triple-negative cell line associated with high-grade, aggressive disease, SCP2, a bone-metastatic subclone of MDA-MB-231 selected in vivo for preferential bone tropism [29], MCF7, an ER-positive luminal A cell line associated with a more indolent phenotype, and BT-474, an ER-positive, PR-positive, HER2/neu-overexpressing luminal B cell line. These subtypes also have different metastatic propensity. Indeed, despite a less aggressive phenotype and less propensity for migration, hormone receptor-positive tumors show a predilection for bones as the first site of relapse compared to hormone-receptor-negative tumors, which have a propensity to develop visceral metastasis [48,49]. Here, we observe that bone ECM induces molecular and phenotypic changes in breast cancer cells. When cultured within a bone-mimetic matrix, all tested cell lines exhibited reduced proliferation compared to those grown in a coll scaffold, indicating an adaptive response to a hostile microenvironment. This observation is consistent with findings by Choi et al., who reported that matrix mineralization promotes the emergence of a less proliferative phenotype in breast cancer cells [50]. Such behavior likely reflects a survival mechanism in response to environmental stressors characteristic of the mineralized bone niche [51]. Although all cell lines displayed reduced proliferation within the coll-HA scaffold, their subsequent adaptive responses differed according to molecular subtype. This indicates that exposure to the same ECM context does not elicit a uniform response but rather reveals lineage-dependent programs of adaptation. Triple negative breast cancer cells, MDA-MB-231 and SCP2, when cultured in coll-HA scaffold undergo a partial MET [52], confirmed by the acquisition of an epithelial-like morphology, a decreased proliferation and the upregulation of epithelial markers alongside the downregulation of mesenchymal markers. In particular, the concurrent downregulation of MYC and HIF-1α signalings indicates a coordinated suppression of proliferative and hypoxia-driven EMT programs, which may contribute to epithelial stabilization. This reversion has been demonstrated to be fundamental for the colonization of metastatic sites and the establishment of subsequent metastasis [53]. While EMT [54,55] is necessary to escape from the primary tumor, these cells must revert to an epithelial state to successfully colonize an organ [56,57]. In contrast, MCF7 cells, luminal A breast cancer cells that inherently exhibit an epithelial phenotype, not only demonstrated reduced proliferation but also showed a marked upregulation of mesenchymal markers and a loss of CDH1 expression, indicative of a transition toward a mesenchymal phenotype. This phenotypic shift warrants further investigation as it may be associated with the acquisition of a dormant phenotype in the bone niche, which is characteristic of luminal breast cancer [58,59]. Dormancy in this context may serve as a survival strategy, characterized by a reversible growth arrest in which cells enter a quiescent, non-proliferative state with reduced metabolic activity, altered gene expression profiles, and increased resistance to conventional therapies. This allows tumor cells to evade immune surveillance, potentially contributing to late metastatic relapse [60]. To better understand the molecular basis of these phenotypic differences, we examined transcriptional changes induced by the coll-HA scaffolds. RNA sequencing data revealed that bone-mimetic ECM induces modulation of bone remodeling and metabolic pathways, underscoring the adaptive responses of cancer cells to this microenvironment. Regardless of the subtype, we observed a significant downregulation of the SLIT and ROBO pathway induced by the bone-mimetic matrix, compared to the collagen one. This signaling participates in the maintenance of bone metabolism by inhibiting osteoclasts formation and activity and promoting bone formation [35]. This suggests that the bone-mimetic matrix can modulate bone-related pathways involved in bone remodeling toward an increase in osteoclasts formation. We next focused on metabolic pathways, recognizing that metabolic rewiring is a key enabler of metastatic progression and may arise in response to environmental stressors such as hypoxia and nutrient deprivation [61]. Our findings reveal a complex picture. While previous studies have shown that amino acid and selenoamino acid metabolism support metastasis [62] and are upregulated in bone-tropic breast cancer cells [63], our data indicates that these pathways are significantly downregulated in SCP2 and MCF7 cells cultured in coll-HA scaffolds. This apparent contradiction may in fact reflect a context-dependent adaptation. The downregulation of amino acid and selenoamino acid metabolism in our models is consistent with a cellular response aimed at conserving energy and resources. In a bone-mimetic microenvironment, characterized by limited oxygen and nutrient availability, reducing protein synthesis and metabolic activity may enhance cellular survival. This interpretation is further supported

by the concurrent downregulation of the ribosome pathway observed across all four cell lines, and by the associated reduction in proliferation rates. It is important to note that this analysis considers only the role of the extracellular matrix. In vivo, interactions with bone-resident cells such as osteoblasts, osteoclasts, and immune cells may further influence metabolic adaptation and could account for some of the discrepancies with other published findings. Interestingly, MCF7 cells demonstrated a distinct adaptation strategy by upregulating lipid metabolism, the TCA cycle, and the respiratory electron transport chain. This shift toward mitochondrial respiration and lipid oxidation is aligned with previous reports linking these pathways to enhanced metastatic potential and survival in hostile microenvironments [64,65]. Together these findings highlight that exposure to the bone-mimetic matrix coincided with breast cancer cells undergoing specific, lineage-dependent metabolic reprogramming. These metabolic shifts may not only facilitate survival and dormancy in bone but also represent potential therapeutic vulnerabilities. On the other hand, transcriptional programs related to matrix interaction and remodeling were found to be primarily influenced by the transition to a three-dimensional environment, with no significant additional effect of scaffold mineralization. The phenotypic and molecular differences observed in the coll-HA scaffold were accompanied by changes in responsiveness to clinically relevant bone-targeted therapies (Zoledronic Acid, Denosumab). Despite the subtype, all the cell lines show a significantly increased sensitivity to Zol and Deno when cultured in coll-HA scaffolds. This finding, along with the specific modulation of inflammatory cytokines and RANKL, suggests that a bone-mimetic milieu can increase tumor cell susceptibility to bone-targeted therapies, a phenomenon that may also occur in vivo during bone metastasis. Supporting this, previous studies have shown that RANKL expression is markedly higher in breast cancer metastasis to bone compared with primary tumors [66]. Enhanced sensitivity to Deno may be associated by the increased RANKL expression observed in 3D scaffolds, particularly in the coll-HA culture condition. The higher response to Zol is likely mediated by mechanisms independent of the RANK/RANKL axis. Notably, HA is known to exhibit a high affinity for bisphosphonates [67]; thus, its presence within the scaffold may enhance local Zol accumulation and prolong cellular exposure, thereby potentiating its anti-tumor activity. Investigating how these sensitivities are modulated within different microenvironments could reveal potential strategies to enhance treatment efficacy.

The influence of the bone ECM extended beyond cancer cells themselves. Because metastatic progression depends on reciprocal interactions between tumor cells and the bone microenvironment, we investigated whether ECM-induced tumor cell reprogramming also affected osteoclast differentiation and therapeutic responsiveness. When cultured in both 3D models, breast cancer cells upregulate the release of soluble factors, like IL-6 and IL-8, involved in the osteoclast differentiation and activation compared to the monolayer, in a matrix- and lineage-specific fashion, inducing a pro-tumorigenic bone environment [69]. Moreover, depending on the CM, osteoclasts exhibited resistance either to Zol or to Deno. Differences in cytokine composition among culture conditions may shift osteoclast dependence on specific differentiation signaling pathways, thereby altering treatment sensitivity. This suggests that spatial organization, cellular confinement and matrix composition within a 3D context may play a key role in regulating cytokine expression, potentially by influencing factors that are not recapitulated in traditional 2D cultures. Such insights underscore the importance of 3D models in faithfully mimicking in vivo tumor biology. These results also support the hypothesis that breast cancer cells modulate bone cells also at early stages, creating a pre-metastatic niche conducive to subsequent colonization [68,69]. Also, they outline that tumor-ECM interactions can amplify osteolysis, contributing to disease progression. Notably, BT-474 exhibited no osteoclastogenic potential and no sensitivity to bone targeted drugs. This finding is consistent with the infrequent use of BT-474 in bone metastasis models and aligns with previous in vivo xenograft studies reporting predominantly osteoblastic bone growth rather than osteolytic remodeling [70]. Collectively, these observations further underscore the validity of our model in accurately capturing differences between breast cancer subtypes and indicate that BT-474 may have restricted relevance for modeling osteoclast-driven bone metastasis and for evaluating therapeutics targeting bone resorption pathways.

This study has two main contributions. First, we developed and validated a biomimetic collagen–hydroxyapatite scaffold that reproduces key structural, physicochemical and mechanical characteristics of the bone tissue establishing a platform to investigate ECM-dependent regulation of breast cancer cell behavior [71]. The novelty and added value of our model lies in its flexibility and adaptability which enables the mimicking of different organo-specific microenvironments by modulating the scaffold properties and composition. Second, by using this platform, we identified subtype-dependent differences in how breast cancer cells adapt to a bone-like environment, affecting cell plasticity, molecular programs, osteoclast-related functions and responsiveness to bone-targeted therapies. Importantly, validation against primary breast cancer bone metastasis samples confirmed that this scaffold model faithfully recapitulates key expression patterns associated with bone metastasis, supporting its use for investigating underlying molecular mechanisms. Together, these findings support the use of organo-specific ECM models to investigate microenvironment-dependent mechanisms of bone metastasis. The modular and scalable design of the scaffolds will enable its adaptation to high-throughput drug screening and, when combined with patient-derived cells, offers the potential to evaluate patient-specific responses to bone-targeted therapies.

This study has some limitations that should be considered. Although the coll-HA scaffold reproduces key structural, physicochemical and mechanical features of the bone ECM, it is designed to model selected aspects of the bone metastatic niche and therefore does not fully capture its biological complexity. In particular, the present system isolate the contribution of the extracellular matrix and therefore does not include the dynamic interactions with bone-resident cells, such as osteoblasts, osteoclasts, endothelial, stromal and immune cells, which are known to influence metastatic progression. Moreover, while the comparison between coll and coll-HA matrices demonstrates that organo-specific ECM is associated with distinct adaptive responses, the individual contributions of matrix composition, architecture and mechanical properties cannot be fully distinguished in the current model. Future studies should further refine the model by incorporating additional ECM components such as bone-resident cells, and by independently tuning the biomaterial properties, to enable a more comprehensive understanding of the relative contribution of matrix and stromal composition, architecture and mechanics to breast cancer adaptation within the bone niche.

4. Material and methods

4.1. 3D coll and 3D coll-HA scaffold synthesis

Coll scaffolds were synthesized as follows: a 1 wt% suspension of type I collagen (Cod. C9879 Sigma Aldrich) in acetic acid was prepared and precipitated to pH 5.5. The material was cross-linked through a 1 wt % BDDGE (Cat. 220,892 Sigma Aldrich) to stabilize the collagen matrix and to control porosity. Scaffold's porosity and pore size were obtained through an optimized freeze-drying process, consisting of an established freezing and heating ramp (from 25 °C to −25 °C and from −25 °C to 25 °C in 50 min under vacuum conditions, $p = 0.20$ mbar), ultimately ensuring proper pore interconnectivity and orientation. For coll-HA scaffolds, collagen solution was mixed and cross-linked with hydroxyapatite (Cod. 677,418 Sigma Aldrich) in a ratio of 30:70 respectively, to mimic the healthy bone structure since the bone matrix is composed of 30% of collagen and 70% of minerals. All scaffolds were sterilized by immersion in 70% ethanol for 1 h, followed by three washes in sterile Dulbecco Phosphate Buffered Saline (DPBS) (Thermo Fisher Scientific,

Waltham, MA USA).

4.2. Field-emission scanning electron microscopy (FE-SEM)

FE-SEM of 3D coll-HA scaffold was performed by a ZEISS GeminiSEM500 at 5 kV. The sample was placed on specimen stubs and coated with gold by sputtering with an AGAR Auto Sputter Coater. Before the measurement, the sample was deposited with a chromium thin film (5 nm) by sputter-coating using a QUORUM Q 150 T ES plus coater.

4.3. Attenuated total reflection Fourier transform infrared (ATR-FTIR) spectroscopy

ATR-FTIR spectroscopy of 3D coll-HA scaffold was performed at room temperature, by using Agilent Cary 630 FTIR spectrometer equipped with an ATR-IR cell (UATR unit cell). IR spectra were recorded by averaging 32 scans, with a resolution of 4 cm^{-1}.

4.4. X-Ray Diffraction (XRD)

Powder XRD patterns were obtained using a D8 Discover diffractometer in reflection mode with Cu Kα radiation (45 kV, 40 mA). The crystallinity degree (X_C) was calculated with Equation X, where V112/300 described the minimum intensity between two reflections from crystal planes (112) and (300) and I300 was the intensity reflection for plane (300). The mean crystalline size (X_{hkl}) was calculated with the line broadening of the (211) reflection (Equation X), where X_{hkl} is the crystallite size (nm), λ is the wavelength of monochromatic X-ray beam (nm) (λ = 0.15418 nm for CuKα radiation), β ½ is the full width at half maximum for the diffraction peak under consideration (rad), 'θ' is the diffraction angle (°), and 'K' is a constant varying with crystal habit and chosen to be 0.9. Interplanar distance for the lattice spacing of (211) was calculated with Equation X.

$$Xc = 1 - \frac{V_{112\backslash 300}}{I_{300}}$$

$$Xhkl = K\lambda / \beta_{1/2}\, Cos\theta$$

$$2d\sin\theta = n\lambda$$

4.5. Swelling and stability

Scaffolds were incubated in PBS at 37 °C, and their weight at different timepoints was recorded. Swelling was calculated as the ratio between the wet hydrogel mass (w_{wet}) and the initial, dry weight (w_{dry}).

Scaffolds were incubated in PBS at 37 °C, lyophilized overnight to record the dry weight and rehydrated in PBS at 37 °C. The experiment was conducted for 28 days, recording the dry weight at different timepoints. Stability was calculated as the ratio between the dry weight at each timepoint (w_{dry}) and the initial dry weight ($w_{dry,0}$).

4.6. MicroCT imaging (μCT)

Samples were imaged using the SkyScan 1172 high-resolution *μCT* system (Bruker; hardware version F). The machine was equipped with a Hamamatsu 100/250 X-ray source and an 11-megapixel Hamamatsu C9300 CCD camera. In the case of coll-HA scaffolds, scans were acquired at 48 kV and 200 μA, using a 0.5 mm aluminum filter to reduce beam hardening. On the other hand, coll scaffold images were acquired at 48 kV and 167 μA, without the use of an external filter. The voxel size in both cases was 6.85 μm. A step-and-shoot acquisition protocol was used with a 0.30° rotation step, covering a total angular range of 192.6° (counter-clockwise rotation). Frame averaging (4×), random movement (10), flat-field correction, geometrical correction, and median filtering were applied during acquisition to improve signal-to-noise ratio. Lastly, reconstruction was performed using NRecon v1.7.4.2 (NReconServer engine v1.7.4), followed by 3D volume rendering and analysis using Dragonfly software, Version 2022.2 (Object Research Systems Inc).

4.7. Leachate assay

Gas chromatography–mass spectrometry (GC–MS) was employed to investigate residual BDDGE in washing waters and leachates from coll and coll-HA scaffolds, following a previously reported protocols for BDDGE cross-linked collagenous matrices [72]. GC–MS analyses were carried out using a PerkinElmer Clarus 690 gas chromatograph coupled to a Clarus SQ8 T single quadrupole mass spectrometer, operated in electron ionization (EI) mode at 70 eV. The GC system was equipped with a (5%- phenyl)-methylpolysiloxane capillary column (30 m × 0.25 mm i.d., 0.25 μm film thickness). The injector temperature was set at 250 °C and operated in split mode (1:10). The ion source and transfer line temperatures were maintained at 200 °C and 280 °C, respectively. Hydrogen was used as the carrier gas at constant flow. Mass spectra were acquired in full scan mode over the *m/z* range 50–650, with a solvent delay of 2.8 min. Chromatographic separation was achieved using the following oven temperature program: 100 °C for 2 min, ramp at 10 °C·min^{-1} to 250 °C (20 min), followed by a ramp at 5 °C·min^{-1} to 280 °C (25 min). A reference solution of BDDGE in ethyl acetate was analyzed under identical GC–MS conditions to establish its retention time and EI fragmentation pattern, which were used as diagnostic criteria for compound identification. BDDGE identification was based on retention time matching and on the characteristic EI mass spectrum dominated by fragment ions at m/z 57 (base peak), 69, 73, and 129, in agreement with NIST library data and literature reports.

4.8. Mechanical properties

Compression testing was performed using an Instron 6800 Series Universal Testing System, equipped with a 100 N load cell. Scaffolds measuring 10 mm in diameter and 1.8 mm in height were compressed at 1 mm/min displacement rate. The test was terminated at 100% compression or 97 N force, the latter to prevent damaging the load cell. The Young's modulus was calculated as the slope of the stress-strain curve in the linear region (30% strain).

4.9. Tumor cell seeding and culture

The experiments were performed on four human breast cancer cell lines: the triple negative cell line MDA-MB-231 (obtained from the America Type Culture Collection, ATCC, Rockville, Maryland, USA), the SCP2 cell line, an osteotropic cell line originating from MDA-MB-231 kindly provided by Yibin Kang's laboratory, the hormonal receptor positive MCF7, obtained from ATCC, and BT-474 representative of the estrogen receptor positive, progesterone receptor-positive, and HER2/neu overexpressing luminal B breast cancer subtype. All cells were maintained in DMEM medium supplemented with 10% fetal bovine serum, 1% penicillin-streptomycin and 1% glutamine at 37 °C in a 5% CO2 atmosphere. For standard cultures, $1 \times 10^{\hat{}}6$ cells were maintained as a monolayer in 25 cm^2 flasks in 4 mL of culture medium. For 3D cultures, each scaffold (2 × 9 mm) was placed in a 6-multiwell plate and seeded with $1 \times 10^{\hat{}}6$ cells by adding 50 μL of cell suspension on the scaffold upper surface. Seeding was reached by simple soaking of the cell suspension in the dry scaffolds. Cells were incubated for 1 h at 37 °C to allow adhesion, after that 4 mL of culture medium were carefully added. After 24 h, the scaffolds were gently moved in a new 6-multiwell plate to avoid any contribution of cells that might have attached on the plate surfaces. The medium was replaced every two days.

4.10. IHC staining

Scaffolds have been washed with PBS and fixed in 4% formalin overnight at 4 °C. The day after samples were processed for paraffin embedding. 4 μm thick histological sections were obtained by formalin-fixed, paraffin-embedded tumor samples and stained with hematoxylin & eosin (H&E) in an automatic slides stainer. Paraffin-embedded bone metastatic tissue was collected and cleared in 4 μm thick sections. Staining with H&E was performed. Samples were collected retrospectively under the study protocol approved by IRST-Area Vasta Romagna Ethics Committee (approval no. 4751, 31 July 2015, Amendment 1 05/10/2016). All the procedures were performed in accordance with GCP and Helsinki declaration. Stained sections were digitized using the Aperio scanning system (Leica Biosystems) for detailed histological analysis.

4.11. Osteoclastogenesis assay

Human osteoclasts were obtained from the differentiation of peripheral blood mononuclear cells (hPBMCs) of healthy donors who gave written informed consent to take part in the study. Monocytes were isolated from buffy coats by Lymphosep™ density gradient [73]. Briefly, EDTA whole blood (50 mL) was diluted 1:1 with phosphate-buffered saline (PBS), layered on lymphocyte separation medium (Lymphosep™, Biowest LLC, Riverside, MO, USA) and centrifuged without brakes at 2200 rpm for 10 min. The hPBMCs layer was collected and washed twice with PBS and treated for 4 min on ice with ACK solution. After having washed them twice with phosphate-buffered saline, cells were suspended in complete α-MEM (LONZA, Basel, Switzerland). Cells were counted and plated at a concentration of $1.5 \times 10^{\hat{}6}$ PBMCs per 2 $cm^{\hat{}2}$/well. After 4 h, the medium was removed and differentiation into osteoclasts was induced by α-MEM supplemented with 20 ng/mL of M-CSF (Cod. 300–25; Peprotech, Rocky Hill, NJ, USA). From Day 7 of culture, RANKL (20 ng/mL) (Cod. 310–01; Peprotech, Rocky Hill, NJ, USA) was added with M-CSF (control positive condition, Ctrl+). The medium was changed every 2–3 days and TRAP+ multinucleated cells were observed after 15 days of differentiation. Each condition was performed in triplicate and experiments were run at least three times. Schematic Representation in Fig. S6a.

4.12. Indirect co-culture of tumor cells and osteoclasts

To evaluate tumor cells' effects on osteoclasts differentiation, indirect co-culture was optimized by adding in osteoclasts' medium culture 20% of CM by breast cancer cell lines (schematic representation in Fig. S6a). CM was collected at 7 days of breast cancer cells' culture in 2D or 3D models. Briefly, cancer cells were seeded at a concentration of $1 \times 10^{\hat{}6}$ cells per 25 cm^2 in a 2D model or in 3D scaffolds. Then, cells were cultured in α-MEM complete medium and at day 6th medium was replaced with fresh medium and collected at day 7th.

4.13. Quantification of TRAP-positive multinucleated cells

Differentiated osteoclasts, cultured in 2D plates, were fixed after 15 days of differentiation by incubation in 4% Paraformaldehyde (PFA, Electron Microscopy Sciences, Hatfield, PA, USA) for 20 min at room temperature and then stained for tartrate resistant acid phosphate staining (TRAP kit, Cod. 3879 A; Sigma-Aldrich, Darmstadt, Germany). Osteoclasts were counted with a magnification of 10× in Nikon Eclipse Ci microscope in 5 fields/well as multinucleated cells (more than 4 nuclei) TRAP-positive cells. Images of differentiated osteoclasts were acquired at different magnifications with Nikon Eclipse Ci microscope. Each experiment was performed in triplicate and repeated at least three times.

4.14. Tumor cell growth assay

Tumor cell growth was assessed by MTT assay. Briefly, at different time points cells within the scaffolds or in monolayer cultures were incubated with 0.5 mg/mL of MTT solution (Sigma Aldrich, Darmstadt, Germany) in PBS for 2 h at 37 °C and the absorbance was determined at 550 nm with a multimode microplate reader, BioTek Synergy H1 (Agilent).

To determine metabolically active cells, the CellTiter-Glo® 3D assay (Promega) was performed. Briefly, the scaffold with 500 μL of culture media were transferred into a new plate and 500 μL of CellTiter-Glo® 3D reagent was added into each well. Plates were protected from light and shaken for 5 min (room temperature) to induce cell lysis. Samples were incubated for additional 25 min in the dark, at room-temperature, to stabilize the bioluminescent signal. The luminescence was recorded by a multimode microplate reader, BioTek Synergy H1 (Agilent).

4.15. Drug exposure and dose selection

Zoledronic Acid (Zol, Zometa®), was solubilized at a concentration of 50 mM in sterile water, filtered and stored at −20 °C. Denosumab (Deno) 120 mg in 1.7 mL (XGEVA®) was stored at 4 °C. Drugs were diluted in complete α-MEM. Doses of Zol and Deno were selected based on plasma levels from pharmacokinetic clinical data. We used 24 μg/mL concentration for Deno and 10 μM for Zol, as it was reported to accumulate in bone tissues at a higher concentration than plasmatic peak [67]. Osteoclasts were treated with Deno and Zol for 72 h at day 7 (in the latest stages of osteoclasts differentiation). To determine osteoclastogenesis inhibition, the number of osteoclast cells in treated wells was normalized to untreated wells. Inhibition of osteoclastogenesis after drug exposure was reported as percentage (%) of osteoclastogenesis normalized to the untreated control (schematic representation in Fig. S6b).

4.16. Immunofluorescence staining

For immunofluorescence staining, cells were fixed 20 min in 4% PFA and permeabilized with PBS + 1% BSA + 0.3% Triton X-100. Then, cells were stained with Phalloidin antibody (Alexa Fluor™ Phalloidin; Life Technologies) to detect filamentous actin (F-actin). Dapi staining was used to counterstain the nucleus. In addition, the following antibodies were used: CD254 (RANKL) -PE (Miltenyi Biotec) and CD265 (RANK) -APC (Miltenyi Biotec) each at a dilution of 1:200 in PBS with 1% BSA. Antibody incubation was performed for 2 h at room temperature, followed by Phalloindin and Dapi staining. Images were taken by Nikon A1R laser confocal microscope N-SIM technology (Nikon Corporation, Tokyo, Japan) at 20× or 40× of magnification. The images were then analyzed using ImageJ software (Version 1.52a) by selecting one cell at a time in an image and measuring the area, perimeter and integrated density. For the fluorescence intensity of RANKL positivity, four different areas were randomly selected in five different images, and the median of integrated density was calculated by Excel, for each condition. Fluorescence intensity for RANKL positivity in 2D cultured cells was used as the normalizing reference for 3D conditions.

Based on Phalloidin positivity, the circularity of tumor cells was calculated. For each image, at least eighty cells were randomly selected, drawing the perimeter, and calculating area and perimeter. Three images for each condition were analyzed. The circularity was calculated through the expression [74]:

$$Circularity = \frac{4\pi A}{2p^2}$$

The cells were divided in two groups based on the following ranges: circularity <0.4, indicating a spindle-like morphology, and circularity between 0.4 and 0.7 indicating an epithelial-like morphology [75].

4.17. Quantitative real time reverse transcription PCR (qRT-PCR)

The scaffolds were fragmented into small pieces, while 2D culture cells were collected by trypsinization. Total mRNA was isolated using TRIzol Reagent (Invitrogen) following the manufacturer's instructions. Five hundred nanograms of RNA were reverse transcribed using the iScript cDNA Synthesis Kit (BioRad, Hercules, CA, USA). The final mixture was incubated at 25 °C for 5 min, at 42 °C for 20 min, at 47 °C for 20 min, at 50 °C for 15 min and 5 min at 85 °C. Real-Time PCR was performed on the 7500 Real-Time PCR System (Applied Biosystems, Waltham, MA, USA) using the TaqMan gene expression assay mix (Applied Biosystems, Waltham, MA, USA). Amplification was performed from 2 μL of cDNA, in a final volume of 20 μL containing 2× Gene expression master Mix (Applied Biosystems, Waltham, MA, USA). The stably expressed endogenous HPRT was used as a reference gene. The following markers were analyzed: *E*-Cadherin (CDH1), Vimentin (VIM), SNAI1, SNAI2, ZEB1, ZEB2, CD44, TJP1, THBS1,TNF-α, IL-6, IL-8, RANK and OPG. The amount of transcripts was normalized to the endogenous reference genes and expressed as n-fold mRNA levels relative to a calibrator using a comparative threshold cycle (Ct) value method (ΔΔCt).

4.18. RNA sequencing

RNA-seq libraries were prepared using the Illumina Stranded Total RNA Prep with Ribo-Zero Plus (Illumina, San Diego, CA, USA), starting with 0.5 μg of total RNA. In brief, RNA was subjected to Ribosomal RNA Depletion, then it was fragmented and annealed with random hexamers, which prime the sample for cDNA synthesis. The hexamer-primed RNA was transcribed using both actinomycin-D (during the first-strand cDNA synthesis), and dUTP (during the second-strand synthesis) to achieve strand specificity. Then, the libraries were end-repaired and adenylated before being ligated with single-indexed adapters (IDT for Illumina DNA/RNA UD Indexes Set B; Illumina, San Diego, USA) and amplified by PCR for 12 cycles. The last purification step was performed with Agencourt AMPure XP beads (Beckman Coulter). The prepared libraries were quantified using both Agilent 2100 Bioanalyzer and Invitrogen Qubit Fluorometer and pooled in equimolar amounts. Sequencing was performed on Illumina NextSeq 550 System using NextSeq 500/550 High-Output v2.5 Kit - 150 cycles (Illumina, San Diego, CA, USA). Raw sequencing reads were quality-controlled using FastQC and MultiQC, then processed to remove adapter sequences and low-quality bases using trimming software. Tables S1 and S2 summarize the number of biological replicates, sequencing depth, and mapping quality metrics. The pre-processed reads were pseudo-aligned and quantified using Kallisto using the GRCh38 transcriptome. Read counts were analyzed using the DESeq2 R package to detect differentially expressed genes (DEGs) with an adjusted *P*-value (p-adj) less than 0.05. Gene Set Enrichment Analysis was performed with clusterProfiler (R package). All graphical representations were performed using ggplot2, EnhancedVolcano and complexHeatmap (R packages). Transcription factor (TF) activity was inferred using the decoupleR R package (v2.12.0). Differential expression results from the coll-HA vs coll comparison were first obtained using DESeq2, and the Wald test statistic (stat) was used as input for TF activity inference. TF–target interactions were derived from the DoRothEA regulons as implemented in decoupleR, restricting the analysis to high- and medium-confidence interactions (confidence levels A, B, and C). TF activity scores were computed using the VIPER method, which infers regulator activity based on the coordinated enrichment of signed TF targets within the differential expression signature. Regulons were required to contain a minimum of 25 expressed target genes to ensure robust activity estimation. *P*-values were adjusted for multiple testing using the Benjamini–Hochberg procedure, and TFs with an adjusted *p*-value <0.05 were considered statistically significant [76].

4.19. Statistical analysis

Each experiment was performed in at least three biological replicates, with three technical replicates per condition. Data are presented as mean ± SD (standard deviation) or as percentage (%) of osteoclastogenesis or percentage (%) of survival. GraphPad Prism was used to perform all statistics. The differences between groups were assessed by two-tailed Student's *t*-test, Mann-Whitney test, or one-way/two way ANOVA followed by Tukey's post hoc test for multiple comparison as appropriated, and accepted as significant when $^{*}P < 0.05$.

5. Conclusion

In conclusion, our study highlights the fundamental role of the ECM in regulating cancer cell behavior and indicates the utility of our model in elucidating its multifaceted contributions to tumor metastasis. Our findings show that the bone mineral matrix induces in breast cancer cells specific metabolic shifts, alters drug responses, and drives changes in cellular plasticity-both in terms of proliferation and phenotypic features. This underscores the importance of considering ECM-driven mechanisms in the progression of bone metastasis and highlights the need for advanced in vitro models capable of faithfully recapitulating these interactions. Our 3D bone-biomimetic model provides a powerful platform to dissect the intricate crosstalk between breast cancer cells and the bone microenvironment, offering a valuable tool for identifying key molecular drivers of metastasis and testing microenvironment-targeted therapeutic strategies. While further validation with patient-derived clinical samples is necessary to enhance its translational relevance, this model represents a crucial step toward a more comprehensive understanding of the natural history of breast cancer bone metastasis, capturing the complexity of tumor-ECM interactions.

CRediT authorship contribution statement

Chiara Spadazzi: Writing – original draft, Conceptualization. **Silvia Vanni:** Writing – review & editing, Data curation. **Alessandro De Vita:** Writing – review & editing, Data curation. **Claudia Cocchi:** Writing – review & editing, Data curation. **Sofia Gabellone:** Writing – review & editing, Data curation. **Giacomo Miserocchi:** Writing – review & editing, Data curation. **Chiara Calabrese:** Writing – review & editing, Data curation. **Sofia Dellavalle:** Writing – review & editing, Data curation. **Oneda Cani:** Writing – review & editing, Data curation. **Lucas Moron Dalla Tor:** Writing – review & editing, Data curation. **Michela Tebaldi:** Writing – review & editing, Data curation. **Ane Urigoitia-Asua:** Writing – review & editing, Data curation. **Dorleta Jimenez de Aberasturi:** Writing – review & editing, Data curation. **Erlantz Lizundia:** Writing – review & editing, Data curation. **Oihane Mitxelena-Iribarren:** Writing – review & editing, Data curation. **Amaia Cipitria:** Writing – review & editing, Data curation. **Antonino Musolino:** Writing – review & editing, Data curation. **Chiara Casadei:** Writing – review & editing, Data curation. **Giulia Sbanchi:** Writing – review & editing, Data curation. **Denisa Toma:** Writing – review & editing, Data curation. **Eliana Capecchi:** Writing – review & editing, Data curation. **Raffaele Saladino:** Writing – review & editing, Data curation. **Toni Ibrahim:** Writing – review & editing. **Laura Mercatali:** Writing – review & editing, Supervision, Conceptualization. **Chiara Liverani:** Writing – review & editing, Supervision, Conceptualization.

Ethics approval and consent to participate

The research protocol was approved by the IRCCS Istituto Romagnolo per lo Studio dei Tumori (IRST) "Dino Amadori" Institutional review board and by the Local Ethics Committees (AVEC and CEROM). The procedures are in accordance with the Helsinki Declaration of 1975, as revised in 2008. Human osteoclasts were obtained from the differentiation of peripheral blood mononuclear cells derived from buffy coats

of healthy donors who gave written informed consent to take part in the study. We conducted a retrospective study to collect fresh primary bone metastasis specimens isolated from breast cancer patients undergoing surgical resection. Three luminal A, one luminal B, and one triple-negative case were obtained. Patients provided written informed consent to participate in the study, and the study was conducted in accordance with institutional ethical guidelines. For patients who could not be re-contacted, the Principal Investigator subscribed to a Declaration of Anonymization (provisions No. 146 of June 5, 2019).

Declaration of Generative AI and AI-assisted technologies in the writing process

In this work generative artificial intelligence (AI) has not been used.

Funding

This work was partly supported thanks to the contribution of Ricerca Corrente by the Italian Ministry of Health.

Declaration of competing interest

The authors declare that they have no known competing financial interests or personal relationships that could have appeared to influence the work reported in this paper.

Acknowledgements

This work was partly supported thanks to the contribution of Ricerca Corrente by the Italian Ministry of Health. The authors thank Dr. Yibin Kang for providing the SCP2 cell line. Supplementary Figures created with BioRender.com (Student Plan license). We gratefully acknowledge Vicomtech for allowing us to use the μCT equipment.

Appendix A. Supplementary data

Supplementary data to this article can be found online at https://doi.org/10.1016/j.cej.2026.179800.

Data availability

The RNA-seq data generated in this study have been deposited and are publicly available at the following link: https://ega-archive.org/studies/EGAS50000001966.

References

[1] American Cancer Society, Breast Cancer Facts & Figures 2022–2024; Cancer Facts & Figures 2023. https://www.cancer.org/content/dam/cancer-org/research/cancer-facts-and-statistics/breast-cancer-facts-and-figures/2022-2024-breast-cancer-fact-figures-acs.pdf, 2023.
[2] N. Harbeck, F. Penault-Llorca, J. Cortes, M. Gnant, N. Houssami, P. Poortmans, K. Ruddy, J. Tsang, F. Cardoso, Breast cancer, Nat. Rev. Dis. Primers. 5 (2019) 66, https://doi.org/10.1038/s41572-019-0111-2.
[3] J.J. Body, G. Quinn, S. Talbot, E. Booth, G. Demonty, A. Taylor, J. Amelio, Systematic review and meta-analysis on the proportion of patients with breast cancer who develop bone metastases, Crit. Rev. Oncol. Hematol. 115 (2017) 67–80, https://doi.org/10.1016/j.critrevonc.2017.04.008.
[4] Y. Gao, I. Bado, H. Wang, W. Zhang, J.M. Rosen, X.H. Zhang, Metastasis organotropism: redefining the congenial soil, Dev. Cell 49 (2019) 375–391, https://doi.org/10.1016/j.devcel.2019.04.012.
[5] R.R. Langley, I.J. Fidler, The seed and soil hypothesis revisited-the role of tumor-stroma interactions in metastasis to different organs, Int. J. Cancer 128 (2011) 2527–2535, https://doi.org/10.1002/ijc.26031.
[6] R.E. Coleman, P. Smith, R.D. Rubens, Clinical course and prognostic factors following bone recurrence from breast cancer, Br. J. Cancer 77 (1998) 336–340, https://doi.org/10.1038/bjc.1998.52.
[7] R.E. Coleman, Clinical features of metastatic bone disease and risk of skeletal morbidity, Clin. Cancer Res. 12 (2006) 6243s–6249s, https://doi.org/10.1158/1078-0432.CCR-06-0931.
[8] W. Zhang, I.L. Bado, J. Hu, Y.W. Wan, L. Wu, H. Wang, Y. Gao, H.H. Jeong, Z. Xu, X. Hao, B.M. Lege, R. Al-Ouran, L. Li, J. Li, L. Yu, S. Singh, H.C. Lo, M. Niu, J. Liu, W. Jiang, X.H. Zhang, The bone microenvironment invigorates metastatic seeds for further dissemination, Cell 184 (2021) 2471–2486.e20, https://doi.org/10.1016/j.cell.2021.03.011.
[9] Y. Huang, H. Wang, X. Yue, X. Li, Bone serves as a transfer station for secondary dissemination of breast cancer, Bone Res. 11 (2023) 21, https://doi.org/10.1038/s41413-023-00260-1.
[10] M. Esposito, T. Guise, Y. Kang, The biology of bone metastasis, Cold Spring Harb. Perspect. Med. 8 (2018) a031252, https://doi.org/10.1101/cshperspect.a031252.
[11] B. Clarke, Normal bone anatomy and physiology, Clin. J. Am. Soc. Nephrol. 3 (2008) S131–S139, https://doi.org/10.2215/CJN.04151206.
[12] X. Lin, S. Patil, Y.G. Gao, A. Qian, The bone extracellular matrix in bone formation and regeneration, Front. Pharmacol. 11 (2020) 757, https://doi.org/10.3389/fphar.2020.00757.
[13] S.R. Stock, The Mineral-Collagen Interface in Bone, Calcif. Tissue Int. 97 (2015) 262–280, https://doi.org/10.1007/s00223-015-9984-6.
[14] N. Alcorta-Sevillano, I. Macías, A. Infante, C.I. Rodríguez, Deciphering the relevance of bone ECM signaling, Cells 9 (2020) 2630, https://doi.org/10.3390/cells9122630.
[15] V. Poltavets, M. Kochetkova, S.M. Pitson, M.S. Samuel, The role of the extracellular matrix and its molecular and cellular regulators in cancer cell plasticity, Front. Oncol. 8 (2018) 431, https://doi.org/10.3389/fonc.2018.00431.
[16] Y. Hüsemann, J.B. Geigl, F. Schubert, P. Musiani, M. Meyer, E. Burghart, G. Forni, R. Eils, T. Fehm, G. Riethmüller, C.A. Klein, Systemic spread is an early step in breast cancer, Cancer Cell 13 (2008) 58–68, https://doi.org/10.1016/j.ccr.2007.12.003.
[17] E. Risson, A.R. Nobre, V. Maguer-Satta, J.A. Aguirre-Ghiso, The current paradigm and challenges ahead for the dormancy of disseminated tumor cells, Nat. Cancer 1 (2020) 672–680, https://doi.org/10.1038/s43018-020-0088-5.
[18] T.G. Phan, P.I. Croucher, The dormant cancer cell life cycle, Nat. Rev. Cancer 20 (2020) 398–411, https://doi.org/10.1038/s41568-020-0263-0.
[19] P.I. Croucher, M.M. McDonald, T.J. Martin, Bone metastasis: the importance of the neighbourhood, Nat. Rev. Cancer 16 (2016) 373–386, https://doi.org/10.1038/nrc.2016.44.
[20] L.C. Hofbauer, A. Bozec, M. Rauner, F. Jakob, S. Perner, K. Pantel, Novel approaches to target the microenvironment of bone metastasis, Nat. Rev. Clin. Oncol. 18 (2021) 488–505, https://doi.org/10.1038/s41571-021-00499-9.
[21] H. Kolahi Azar, M. Gharibshahian, M. Rostami, V. Mansouri, L. Sabouri, N. Beheshtizadeh, N. Rezaei, The progressive trend of modeling and drug screening systems of breast cancer bone metastasis, J. Biol. Eng. 18 (2024) 14, https://doi.org/10.1186/s13036-024-00408-5.
[22] E.C. González Díaz, S. Sinha, R.S. Avedian, F. Yang, Tissue-engineered 3D models for elucidating primary and metastatic bone cancer progression, Acta Biomater. 99 (2019) 18–32, https://doi.org/10.1016/j.actbio.2019.08.020.
[23] C. Liverani, A. De Vita, S. Minardi, Y. Kang, L. Mercatali, D. Amadori, A. Bongiovanni, F. La Manna, T. Ibrahim, E. Tasciotti, A biomimetic 3D model of hypoxia-driven cancer progression, Sci. Rep. 9 (2019) 1–13, https://doi.org/10.1038/s41598-019-48701-4.
[24] C. Liverani, A. De Vita, C. Spadazzi, G. Miserocchi, C. Cocchi, A. Bongiovanni, A. De Lucia, F. La Manna, F. Fabbri, M. Tebaldi, D. Amadori, E. Tasciotti, G. Martinelli, L. Mercatali, T. Ibrahim, Lineage-specific mechanisms and drivers of breast cancer chemoresistance revealed by 3D biomimetic culture, Mol. Oncol. 16 (2022) 921–939, https://doi.org/10.1002/1878-0261.13037.
[25] M. Kawsar, M. Sahadat Hossain, S. Tabassum S, D. Islam, N.M. Bahadur, S. Ahmed, Crystal structure modification of nano-hydroxyapatite using organic modifiers and hydrothermal technique, RSC Adv. 14 (40) (2024) 29665–29674. Published 2024 Sep 18, https://doi.org/10.1039/d4ra03111c.
[26] Y. In, U. Amornkitbamrung, M.H. Hong, H. Shin, On the crystallization of hydroxyapatite under hydrothermal conditions: role of sebacic acid as an additive, ACS Omega 5 (42) (2020) 27204–27210. Published 2020 Oct 16, https://doi.org/10.1021/acsomega.0c03297.
[27] H. Xie, S. Ruan, M. Zhao, J. Long, X. Ma, J. Guo, X. Lin, Preparation and characterization of 3D hydroxyapatite/collagen scaffolds and its application in bone regeneration with bone morphogenetic protein-2, RSC Adv. 13 (33) (2023 Jul 31) 23010–23020, https://doi.org/10.1039/d3ra03034b.
[28] X. Chen, R. Hughes, N. Mullin, R.J. Hawkins, I. Holen, N.J. Brown, J.K. Hobbs, Atomic force microscopy reveals the mechanical properties of breast cancer bone metastases, Nanoscale 13 (43) (2021 Nov 11) 18237–18246.
[29] A.J. Minn, Y. Kang, I. Serganova, G.P. Gupta, D.D. Giri, M. Doubrovin, V. Ponomarev, W.L. Gerald, R. Blasberg, J. Massagué, Distinct organ-specific metastatic potential of individual breast cancer cells and primary tumors, J. Clin. Invest. 115 (2005) 44–55, https://doi.org/10.1172/JCI22320.
[30] E.Y. Chen, C.M. Tan, Y. Kou, Q. Duan, Z. Wang, G.V. Meirelles, N.R. Clark, A. Ma'ayan, Enrichr: interactive and collaborative HTML5 gene list enrichment analysis tool, BMC Bioinformatics 14 (2013) 128, https://doi.org/10.1186/1471-2105-14-128.
[31] M.V. Kuleshov, M.R. Jones, A.D. Rouillard, N.F. Fernandez, Q. Duan, Z. Wang, S. Koplev, S.L. Jenkins, K.M. Jagodnik, A. Lachmann, M.G. McDermott, C. D. Monteiro, G.W. Gundersen, A. Ma'ayan, Enrichr: a comprehensive gene set enrichment analysis web server 2016 update, Nucleic Acids Res. 44 (2016) W90–W97, https://doi.org/10.1093/nar/gkw377.
[32] Z. Xie, A. Bailey, M.V. Kuleshov, D.J.B. Clarke, J.E. Evangelista, S.L. Jenkins, A. Lachmann, M.L. Wojciechowicz, E. Kropiwnicki, K.M. Jagodnik, M. Jeon, A. Ma'ayan, Gene set knowledge discovery with Enrichr, Curr. Protoc. 1 (2021) e90, https://doi.org/10.1002/cpz1.90.
[33] A. Subramanian, P. Tamayo, V.K. Mootha, S. Mukherjee, B.L. Ebert, M.A. Gillette, A. Paulovich, S.L. Pomeroy, T.R. Golub, E.S. Lander, J.P. Mesirov, Gene set

enrichment analysis: a knowledge-based approach for interpreting genome-wide expression profiles, Proc. Natl. Acad. Sci. U. S. A. 102 (2005) 15545–15550, https://doi.org/10.1073/pnas.0506580102.
[34] S. Bartlome, C.C. Berry, Recent insights into the effects of metabolism on breast cancer cell dormancy, Br. J. Cancer 127 (2022) 1385–1393, https://doi.org/10.1038/s41416-022-01869-5.
[35] V.K. Mootha, C.M. Lindgren, K.F. Eriksson, A. Subramanian, S. Sihag, J. Lehar, P. Puigserver, E. Carlsson, M. Ridderstråle, E. Laurila, N. Houstis, M.J. Daly, N. Patterson, J.P. Mesirov, T.R. Golub, P. Tamayo, B. Spiegelman, E.S. Lander, J. N. Hirschhorn, D. Altshuler, L.C. Groop, PGC-1α-responsive genes involved in oxidative phosphorylation are coordinately downregulated in human diabetes, Nat. Genet. 34 (2003) 267–273, https://doi.org/10.1038/ng1180.
[36] Y. Hu, W. Xu, H. Zeng, Z. He, X. Lu, D. Zuo, G. Qin, W. Chen, OXPHOS-dependent metabolic reprogramming prompts metastatic potential of breast cancer cells under osteogenic differentiation, Br. J. Cancer 123 (2020) 1644–1655, https://doi.org/10.1038/s41416-020-01040-y.
[37] K. Lontos, J. Adamik, A. Tsagianni, D.L. Galson, J.M. Chirgwin, A. Suvannasankha, The role of semaphorin 4D in bone remodeling and cancer metastasis, Front. Endocrinol. (Lausanne) 9 (2018) 322, https://doi.org/10.3389/fendo.2018.00322.
[38] L. Jiang, J. Sun, D. Huang, Role of slit/robo signaling pathway in bone metabolism, Int. J. Biol. Sci. 18 (2022) 1303–1312, https://doi.org/10.7150/ijbs.66931.
[39] S. Seton-Rogers, Metastases arrive at other organs via bone, Nat. Rev. Cancer 21 (2021) 411, https://doi.org/10.1038/s41568-021-00370-0.
[40] I.L. Bado, W. Zhang, J. Hu, Z. Xu, H. Wang, P. Sarkar, L. Li, Y.W. Wan, J. Liu, W. Wu, H.C. Lo, I.S. Kim, S. Singh, M. Janghorban, A.M. Muscarella, A. Goldstein, P. Singh, H.H. Jeong, C. Liu, R. Schiff, X.H. Zhang, The bone microenvironment increases phenotypic plasticity of ER+ breast cancer cells, Dev. Cell 56 (2021) 1100–1117.e9, https://doi.org/10.1016/j.devcel.2021.03.008.
[41] Y. Huang, H. Wang, X. Yue, X. Li, Bone serves as a transfer station for secondary dissemination of breast cancer, Bone Res. 11 (2023) 21, https://doi.org/10.1038/s41413-023-00260-1.
[42] J. Whitburn, C.M. Edwards, Metabolism in the tumour-bone microenvironment, Curr. Osteoporos. Rep. 19 (2021) 494–499, https://doi.org/10.1007/s11914-021-00695-7.
[43] M. Tandon, A.H. Othman, M. Winogradzki, J. Pratap, Bone metastatic breast cancer cells display downregulation of PKC-ζ with enhanced glutamine metabolism, Gene 775 (2021) 145419, https://doi.org/10.1016/j.gene.2021.145419.
[44] W.H. Abuwatfa, W.G. Pitt, G.A. Husseini, Scaffold-based 3D cell culture models in cancer research, J. Biomed. Sci. 31 (1) (2024) 7, https://doi.org/10.1186/s12929-024-00994-y.
[45] J. Redmond, H.O. McCarthy, P. Buchanan, T.J. Levingstone, N.J. Dunne, Development and characterisation of 3D collagen-gelatin based scaffolds for breast cancer research, Biomater. Adv. 142 (2022) 213157, https://doi.org/10.1016/j.bioadv.2022.213157.
[46] Y. Chen, D. Xue, D. Huang, X. Li, Y. Duan, B. Chen, Biofabrication of tunable 3D hydrogel for investigating the matrix stiffness impact on breast cancer chemotherapy resistance, ACS Biomater Sci. Eng. 11 (3) (2025) 1417–1431, https://doi.org/10.1021/acsbiomaterials.4c01636.
[47] F. He, N.L. Springer, M.A. Whitman, S.P. Pathi, Y. Lee, S. Mohanan, S. Marcott, A. E. Chiou, B.S. Blank, N. Iyengar, P.G. Morris, M. Jochelson, C.A. Hudis, P. Shah, J. A.M.R. Kunitake, L.A. Estroff, J. Lammerding, C. Fischbach, Hydroxyapatite mineral enhances malignant potential in a tissue-engineered model of ductal carcinoma in situ (DCIS), Biomaterials 224 (2019) 119489, https://doi.org/10.1016/j.biomaterials.2019.119489.
[48] A. Pareek, O.P. Singh, V. Yogi, H.U. Ghori, V. Tiwari, P. Redhu, Bone metastases incidence and its correlation with hormonal and human epidermal growth factor receptor 2 neu receptors in breast cancer, J. Cancer Res. Ther. 15 (2019) 971–975, https://doi.org/10.4103/jcrt.JCRT_235_18.
[49] H. Yang, R. Wang, F. Zeng, J. Zhao, S. Peng, Y. Ma, S. Chen, S. Ding, L. Zhong, W. Guo, W. Wang, Impact of molecular subtypes on metastatic behavior and overall survival in patients with metastatic breast cancer: a single-center study combined with a large cohort study based on the Surveillance, Epidemiology and End Results database, Oncol. Lett. 20 (2020) 87, https://doi.org/10.3892/ol.2020.11948.
[50] S. Choi, M.A. Whitman, A.A. Shimpi, N.D. Sempertegui, A.E. Chiou, J.E. Druso, A. Verma, S.C. Lux, Z. Cheng, M. Paszek, O. Elemento, L.A. Estroff, C. Fischbach, Bone-matrix mineralization dampens integrin-mediated mechanosignalling and metastatic progression in breast cancer, Nat. Biomed. Eng. 7 (2023) 1455–1472, https://doi.org/10.1038/s41551-023-01077-3.
[51] A. Pérez-González, K. Bévant, C. Blanpain, Cancer cell plasticity during tumor progression, metastasis and response to therapy, Nat. Cancer 4 (2023) 1063–1082, https://doi.org/10.1038/s43018-023-00595-y.
[52] D. Sinha, P. Saha, A. Samanta, A. Bishayee, Emerging concepts of hybrid epithelial-to-mesenchymal transition in cancer progression, Biomolecules 10 (2020) 1561, https://doi.org/10.3390/biom10111561.
[53] N.P. Gunasinghe, A. Wells, E.W. Thompson, H.J. Hugo, Mesenchymal-epithelial transition (MET) as a mechanism for metastatic colonisation in breast cancer, Cancer Metastasis Rev. 31 (2012) 469–478, https://doi.org/10.1007/s10555-012-9377-5.
[54] T. Celià-Terrassa, C. Bastian, D.D. Liu, B. Ell, N.M. Aiello, Y. Wei, J. Zamalloa, A. M. Blanco, X. Hang, D. Kunisky, W. Li, E.D. Williams, H. Rabitz, Y. Kang, Hysteresis control of epithelial-mesenchymal transition dynamics conveys a distinct program with enhanced metastatic ability, Nat. Commun. 9 (2018) 5005, https://doi.org/10.1038/s41467-018-07538-7.
[55] N.M. Aiello, Y. Kang, Context-dependent EMT programs in cancer metastasis, J. Exp. Med. 216 (2019) 1016–1026, https://doi.org/10.1084/jem.20181827.
[56] M. Esposito, N. Mondal, T.M. Greco, Y. Wei, C. Spadazzi, S.C. Lin, H. Zheng, C. Cheung, J.L. Magnani, S.H. Lin, I.M. Cristea, R. Sackstein, Y. Kang, Bone vascular niche E-selectin induces mesenchymal-epithelial transition and Wnt activation in cancer cells to promote bone metastasis, Nat. Cell Biol. 21 (2019) 627–639, https://doi.org/10.1038/s41556-019-0309-2.
[57] M.K. Jolly, K.E. Ware, S. Gilja, J.A. Somarelli, H. Levine, EMT and MET: necessary or permissive for metastasis? Mol. Oncol. 11 (2017) 755–769, https://doi.org/10.1002/1878-0261.12083.
[58] P. Aouad, Y. Zhang, F. De Martino, C. Stibolt, S. Ali, G. Ambrosini, S.A. Mani, K. Maggs, H.M. Quinn, G. Sflomos, C. Brisken, Epithelial-mesenchymal plasticity determines estrogen receptor positive breast cancer dormancy and epithelial reconversion drives recurrence, Nat. Commun. 13 (2022) 4975, https://doi.org/10.1038/s41467-022-32523-6.
[59] X. Yang, X. Liang, M. Zheng, Y. Tang, Cellular phenotype plasticity in cancer dormancy and metastasis, Front. Oncol. 8 (2018) 505, https://doi.org/10.3389/fonc.2018.00505.
[60] R.R. Gomis, S. Gawrzak, Tumor cell dormancy, Mol. Oncol. 11 (2017) 62–78, https://doi.org/10.1016/j.molonc.2016.09.009.
[61] J.A. Mosier, S.C. Schwager, D.A. Boyajian, C.A. Reinhart-King, Cancer cell metabolic plasticity in migration and metastasis, Clin. Exp. Metastasis 38 (2021) 343–359, https://doi.org/10.1007/s10585-021-10102-1.
[62] B. Karno, D.N. Edwards, J. Chen, Metabolic control of cancer metastasis: role of amino acids at secondary organ sites, Oncogene 42 (2023) 3447–3456, https://doi.org/10.1038/s41388-023-02868-3.
[63] S. Pollari, S.M. Käkönen, H. Edgren, M. Wolf, P. Kohonen, H. Sara, T. Guise, M. Nees, O. Kallioniemi, Enhanced serine production by bone metastatic breast cancer cells stimulates osteoclastogenesis, Breast Cancer Res. Treat. 125 (2011) 421–430, https://doi.org/10.1007/s10549-010-0848-5.
[64] X. Bian, R. Liu, Y. Meng, D. Xing, D. Xu, Z. Lu, Lipid metabolism and cancer, J. Exp. Med. 218 (2021) e20201606, https://doi.org/10.1084/jem.20201606.
[65] X. Luo, C. Cheng, Z. Tan, N. Li, M. Tang, L. Yang, Y. Cao, Emerging roles of lipid metabolism in cancer metastasis, Mol. Cancer 16 (2017) 76, https://doi.org/10.1186/s12943-017-0646-3.
[66] L. Huang, Y.Y. Cheng, L.T. Chow, M.H. Zheng, S.M. Kumta, Tumour cells produce receptor activator of NF-kappaB ligand (RANKL) in skeletal metastases, J. Clin. Pathol. 55 (11) (2002) 877–878, https://doi.org/10.1136/jcp.55.11.877.
[67] H.M. Weiss, U. Pfaar, A. Schweitzer, H. Wiegand, A. Skerjanec, H. Schran, Biodistribution and plasma protein binding of zoledronic acid, Drug Metab. Dispos. 36 (2008) 2043–2049, https://doi.org/10.1124/dmd.108.021071.
[68] Y. Liu, X. Cao, Characteristics and significance of the pre-metastatic niche, Cancer Cell 30 (2016) 668–681, https://doi.org/10.1016/j.ccell.2016.09.011.
[69] N. Rabas, R.M.M. Ferreira, S. Di Blasio, I. Malanchi, Cancer-induced systemic pre-conditioning of distant organs: building a niche for metastatic cells, Nat. Rev. Cancer 24 (2024) 829–849, https://doi.org/10.1038/s41568-024-00752-0.
[70] T.E. Kähkönen, M.I. Suominen, J.H.E. Mäki-Jouppila, J.M. Halleen, A. Tanaka, M. Seiler, J. Bernoulli, Human immune system increases breast cancer-induced osteoblastic bone growth in a humanized mouse model without affecting normal bone, J. Immunol. Res. 2019 (2019) 4260987, https://doi.org/10.1155/2019/4260987.
[71] M. Franchi, Z. Piperigkou, N.S. Mastronikolis, N. Karamanos, Extracellular matrix biomechanical roles and adaptation in health and disease, FEBS J. 291 (2024) 430–440, https://doi.org/10.1111/febs.16938.
[72] J.F. Martucci, J.P. Espinosa, R.A. Ruseckaite, Physicochemical properties of films based on bovine gelatin cross-linked with 1,4-butanediol diglycidyl ether, Food Bioproc. Tech. 8 (8) (2015) 1645–1656, https://doi.org/10.1007/s11947-015-1524-x.
[73] C. Spadazzi, F. Recine, L. Mercatali, G. Miserocchi, C. Liverani, A. De Vita, A. Bongiovanni, V. Fausti, T. Ibrahim, mTOR inhibitor and bone-targeted drugs break the vicious cycle between clear-cell renal carcinoma and osteoclasts in an in vitro co-culture model, J. Bone Oncol. 16 (2019) 100227, https://doi.org/10.1016/j.jbo.2019.100227.
[74] A. Pasqualato, V. Lei, A. Cucina, S. Dinicola, F. D'Anselmi, S. Proietti, M. G. Masiello, A. Palombo, M. Bizzarri, Shape in migration: quantitative image analysis of migrating chemoresistant HCT-8 colon cancer cells, Cell Adh. Migr. 7 (5) (2013) 450–459, https://doi.org/10.4161/cam.26765.
[75] M. Schöchlin, S.E. Weissinger, A.R. Brandes, M. Herrmann, P. Möller, J.K. Lennerz, A nuclear circularity-based classifier for diagnostic distinction of desmoplastic from spindle cell melanoma in digitized histological images, J. Pathol. Inform. 5 (1) (2014) 40, https://doi.org/10.4103/2153-3539.143335.
[76] P. Badia-i-Mompel, J. Vélez Santiago, J. Braunger, C. Geiss, D. Dimitrov, S. Müller-Dott, P. Taus, A. Dugourd, C.H. Holland, R. O Ramirez Flores, J. Saez-Rodriguez, decoupleR: ensemble of computational methods to infer biological activities from omics data, Bioinformatics Adv. (2022), https://doi.org/10.1093/bioadv/vbac016.